Electron and Photon induced Reactions on Nuclei in the Nucleon Resonance Region*

J. Lehr, M. Effenberger and U. Mosel
Institut für Theoretische Physik, Universität Giessen
Heinrich-Buff-Ring 16, D-35392 Giessen, Germany
UGI-99-18

Abstract

We calculate total photon-nucleus and electron-nucleus cross sections $\gamma A \to X$, $eA \to e'X$ and several cross sections on pion and eta production in nuclei in the energy regime between the first and the third resonance region for photon virtualities $Q^2 \leq 1.0$ GeV^2 within a semi-classical BUU transport model. In both cases we discuss the varying influence of several medium modifications on the cross sections for different values of Q^2.

PACS numbers: 25.30.Rw, 25.20.x, 25.20.Lj
Keywords: electron-nucleus reaction, photoabsorption, meson electroproduction, meson photoproduction

1 Introduction

Photonuclear reactions are of interest for the investigation of the in-medium behaviour of hadrons. Especially the properties of the rho meson in nuclear matter have been discussed in the last years, because they may be related to chiral symmetry [1]. Experiments on dilepton production in nucleus-nucleus collisions at SPS energies [2, 3] seem to give evidence for a lowering of the in-medium rho mass. Measurements of the photoabsorption cross section on

*Work supported by DFG, GSI Darmstadt and BMBF

nuclei have shown a disappearance of the $D_{13}(1520)$ resonance [4], which may be explained by the changed rho properties [5].

Furthermore, meson photoproduction reactions allow for a study of the in-medium dynamics of pions and etas, which is closely linked to the behaviour of nuclear resonances at normal nuclear matter density. However, due to the equality of energy and momentum of real photons, the different resonances can only be probed at fixed momentum transfer in the absorption process of the photon.

If one extends the discussion of photonuclear reactions to virtual photons, one can get additional information on the in-medium dynamics of resonances, since energy and momentum can then be chosen independently from each other. Electron-nucleus scattering yields a tool to study such processes, because the properties of the virtual photons can be determined by fixing the kinematics and the scattering angle of the electrons. Up to now, most electron scattering data are confined to reactions on nucleons, whereas measurements on nuclei only focussed on the process $eA \to e'X$ (e.g. [6, 7]) for energies up to the Δ resonance.

There are different discussions of inclusive and exclusive (e, e') reactions on nuclei. In [8, 9], for example, there have been calculations within a Δ-hole model, covering the energy regime of the quasielastic peak and the Δ resonance.

In the present work we consider electron-nucleus reactions from the Δ peak to the third resonance region. We extend the work presented in [10, 11] to virtual photons and also discuss some improvements of in-medium effects in photon-nucleus reactions. Our calculations are based on a semiclassical BUU transport model [12], which has also been used very successfully in the past for the description of heavy-ion collisions [13, 14] up to energies of 2 AGeV and pion-nucleus reactions [15].

We proceed in section 2 by outlining the basic ideas of the BUU model. In section 3 we show our parametrizations of the $\gamma^* N$ cross sections, which we need to calculate the cross sections on the nucleus. In section 4 we present our results for the reactions $\gamma^* A \to X$ and discuss the influence of several medium modifications. We also compare our calculations with data. Furthermore, we discuss modifications of the second resonance region in γA and $\gamma^* A$ reactions. In section 5 we turn to the photo- and electroproduction of pions and etas on nuclei, showing total and differential cross sections on ^{40}Ca. We discuss the Q^2-dependence of the production ratios for pions and etas on different nuclei. We close with a summary in section 6.

2 The BUU Model

Most calculations presented in this work have been performed by using a semi-classical BUU transport model. Here we just want to outline its basic ingredients. For more detailed information the reader is referred to [12].

The model is based upon the BUU equation

$$\partial_t f(\vec{r},\vec{p},t) + \partial H \partial \vec{p} \vec{\nabla}_r f(\vec{r},\vec{p},t) - \partial H \partial \vec{r} \vec{\nabla}_p f(\vec{r},\vec{p},t) = I_{coll}[f] \qquad (1)$$

with

$$H = \sqrt{(m+S)^2 + \vec{p}^2}. \qquad (2)$$

f denotes the single-particle phase space density. For $I_{coll} \equiv 0$ we obtain the Vlasov equation, which describes the time evolution of a many particle system under the influence of a mean field Hamilton function H. The right-hand side is the collision integral, consisting of a gain and a loss term, which accounts for possible collisions between the particles. For a system with different particle species one obtains a transport equation for each species that is coupled to all others via the mean field and the collision integral.

Besides the nucleon the model includes in the non-strange sector the resonances $P_{33}(1232)$, $P_{11}(1440)$, $D_{13}(1520)$, $S_{11}(1535)$, $P_{33}(1600)$, $S_{31}(1620)$, $S_{11}(1650)$, $D_{15}(1675)$, $F_{15}(1680)$, $P_{13}(1879)$, $S_{31}(1900)$, $F_{35}(1905)$, $P_{31}(1910)$, $D_{35}(1930)$, $F_{37}(1950)$, $F_{17}(1990)$, $G_{17}(2190)$, $D_{35}(2350)$, which couple to the channels $N\pi$,$N\eta$,$N\omega$,ΛK, $\Delta(1232)\pi$,$N\rho$,$N\sigma$, $N(1440)\pi$ and $\Delta(1232)\rho$. Furthermore we explicitly propagate the mesons π, η, ρ, ω, ϕ and σ (for the description of correlated $\pi\pi$ pairs with isospin zero). Meson-baryon collisions are mainly described through excitations of intermediate baryonic resonances. Above energies of $\sqrt{s} = 2.6$ GeV (for baryon-baryon collisions) and $\sqrt{s} = 2.2$ GeV (for meson-baryon collisions) we use the string fragmentation model FRITIOF [16].

The initialization of the nucleon phase space density f_N in coordinate space is done according to a Woods-Saxon distribution

$$\varrho(r) = \varrho_0 \left(1 + \exp r - r_0\alpha\right)^{-1}$$

with parameters r_0 and α that are fitted to experimental data. In tab. 1 the parameters r_0, α are given for the nuclei ^{12}C, ^{40}Ca and ^{208}Pb.

In momentum space we use local Thomas-Fermi approximation, which yields a local Fermi momentum

$$p_F(r) = \left(32\pi^2 \varrho(r)\right)^{1/3}. \tag{3}$$

For the effective scalar potential S appearing in eq. (2) we use the expression [17]

$$S(\vec{p}, \varrho) = A\varrho\varrho_0 + B\left(\varrho\varrho_0\right)^{\tau} + 2C\varrho_0 \sum_{I,S} \int d^3p' (2\pi)^3 f(\vec{r}, \vec{p}\,') 1 + \left(\vec{p} - \vec{p}\,'\Lambda\right)^2 \tag{4}$$

with parameters A, B, τ fitted to binding energy, saturation density and compressibility [13]. In this paper we use a hard (momentum independent) EOS with compressibility $K = 380$ MeV and $A = -124.3$ MeV, $B = 71.0$ MeV, $C = 0$, $\tau = 2.0$ and a medium momentum dependent EOS with $K = 290$ MeV, $A = -29.3$ MeV, $B = 57.2$ MeV, $C = -63.5$ MeV, $\tau = 1.76$ and $\Lambda = 2.13$ fm^{-1}.

To take into account that the Δ is less bound inside a nucleus than the nucleons we use the Δ potential

$$U_\Delta(p, \varrho) = 23 S(p, \varrho). \tag{5}$$

The exact Thomas-Fermi groundstate corresponding to a local potential as in eq. (4) is given by a step function in coordinate space: $\varrho(r) = \varrho_0 \Theta(R - r)$. Therefore an initialization of a realistic density profile leads to oscillations. We have checked that our results are not influenced by those oscillations by using a finite range Yukawa potential that gave a practically stable nucleus. We use a local potential because for the calculation of relativistic heavy-ion collisions a numerical realization of a finite range potential is difficult.

2.1 Treatment of Δ absorption

In [10] we have calculated the in-medium width of the $\Delta(1232)$ resonance within our transport model. As usually done in transport calculations, we have used vacuum cross sections and only took into account two-body collisions. As a result the total in-medium width, consisting of the spontaneous decay width and the collisional width, was very close to the vacuum width, because the effects of the reduction of the πN decay width due to Pauli

blocking and the collisional broadening nearly cancelled each other. However, these results are in contradiction to what one knows from calculations within the Δ-hole model [18, 19]. There the Δ-'spreading potential' was from πA scattering determined to be

$$-\mathrm{Im}(V_{sp}) = \Gamma_{coll}2 = (40\ \mathrm{MeV})\varrho\varrho_0. \tag{6}$$

The microscopic calculations of the Δ-self energy in [20] gave also results that are in line with this value. In fig. 1 we compare these collisional widths with our results. The widths are shown as a function of the Δ mass. One sees that our total width (dash-dotted line) is about a factor two smaller than the Δ-hole value. Compared to the Δ-hole model calculation of [20] it is in particular notable that our result for the partial width from the process $N\Delta \to NN$ (dot-dot-dashed line) agrees rather well with what is called 'two-body' contribution (dashed line) in this calculation. The main difference to our calculations therefore stems from the three-body contributions (short-dashed line), which correspond to a process $\Delta NN \to NNN$ in a transport model.

In our calculations we did not explicitly include the three-body channel but just determined a decay probability p according to

$$p = \exp(-\Gamma_{coll}t),$$

where Γ_{coll} here denotes the collisional width without the quasielastic contribution. We have checked this procedure by performing calculations in which we implemented the 'BUU' collision width not via explicit collisions but through this method, which gave practically the same results.

As we will discuss below the momentum differential pion production cross sections at photon energies above the Δ resonance are quite sensitive to the treatment of the Δ absorption.

3 Cross Sections for the eN Process

Working in impulse approximation, we assume the electron to interact only with a single nucleon inside the nucleus via a virtual photon. The differential cross section of the process $eN \to e'X$ in the rest frame of the nucleon is then given by:

$$d\sigma dE' d\Omega = \Gamma\sigma_{\gamma^* N\to X} = \Gamma(\sigma_T + \varepsilon\sigma_L). \tag{7}$$

Here Γ and ε are the flux factor and the degree of longitudinal polarization of the virtual photons. Both quantities are functions of the three independent variables E, E' (energies of the incoming and outgoing photon) and ϑ (scattering angle):

$$\Gamma = \alpha 2\pi^2 E' E s - m_N^2 2 m_N Q^2 11 - \varepsilon \tag{8}$$

$$\varepsilon = 11 + 2\tan^2 \vartheta 2(1 + E - E' Q^2), \quad \varepsilon \in [0, 1]. \tag{9}$$

Q^2 is the negative 4-momentum of the virtual photon:

$$Q^2 = 4EE' \sin^2 \vartheta 2. \tag{10}$$

The cross section $\sigma_{\gamma^* N \to X}$ of the virtual photon interacting with the nucleon consists of contributions from all possible channels. Each one can be divided into two parts σ_T and σ_L, arising from transverse and longitudinal photons and can be written as functions of the photon variables $Q^2, E_\gamma = E - E'$ and ε. In the limit $Q^2 \to 0$, σ_T equals the cross section $\sigma(\gamma N \to X)$ with a real photon in the initial state. In our calculations we take into account one-pion, two-pion and eta production in elementary $\gamma^* N$ reactions. We use the cross sections for γN described in [11] to reproduce the energy dependence and incorporate the Q^2 dependence by introducing form factors, which are fitted to experimental data (see sec. 3.4).

Eq. (7) also contains the part σ_L, which vanishes in the limit $Q^2 \to 0$. It is known that the resonant contributions to σ_L are negligible [21] and that σ_L does not exceed $0.2 \cdot \sigma_T$ in the considered Q^2-range [22]. Therefore, the ε-dependence of the total $\gamma^* N$ cross section (eq. (7)) is very weak. Since there are yet no reliable values for σ_L over a wide Q^2, ε and energy range available, we set $\sigma_L = 0$ and try to fit the form factors in such a way that σ_T alone describes the total cross section $\sigma_{\gamma^* N \to X}$. The weak ε-dependence is accounted for by choosing different fit parameters for the three bins $\varepsilon \geq 0.9$, $0.6 < \varepsilon < 0.9$ and $\varepsilon \leq 0.6$.

3.1 One-Pion Production

$\sigma_T(\gamma^* N \to \pi N)$ can be written in terms of helicity amplitudes [23]:

$$\sigma_T = \int d\Omega |\vec{p}_\pi| 2 q_\gamma \sum_{i=1}^{4} |H_i|^2,$$

where $\vec{p}_\pi$ is the pion momentum in the cms and q_γ is the equivalent photon momentum. An expansion in terms of Legendre polynomials P_l gives the following relationship between the H_i and the transverse partial-wave amplitudes $A_{l\pm}$ and $B_{l\pm}$ ($j = l \pm 1/2$, l: angular momentum of the πN-system):

$$\begin{aligned}
H_1 &= 1\sqrt{2}\sin\theta\cos\theta 2\sum_{l=1}^{\infty}(B_{l+} - B_{(l+1)-})(P_l'' - P_{l+1}'') \\
H_2 &= \sqrt{2}\cos\theta 2\sum_{l=0}^{\infty}(A_{l+} - A_{(l+1)-})(P_l' - P_{l+1}') \\
H_3 &= 1\sqrt{2}\sin\theta\sin\theta 2\sum_{l=1}^{\infty}(B_{l+} + B_{(l+1)-})(P_l'' + P_{l+1}'') \\
H_4 &= \sqrt{2}\sin\theta 2\sum_{l=0}^{\infty}(A_{l+} + A_{(l+1)-})(P_l' + P_{l+1}').
\end{aligned} \tag{11}$$

Here θ denotes the scattering angle in the cms. The partial-wave amplitudes consist of a resonant and a background part. This ensures that interferences between both contributions are taken into account in the cross section. Following [11], we use a Breit-Wigner ansatz for the resonant part:

$$\begin{pmatrix} A_{l\pm}(\sqrt{s}, Q^2) \\ B_{l\pm}(\sqrt{s}, Q^2) \end{pmatrix} = \begin{pmatrix} A_{l\pm}(m_R, Q^2) \\ B_{l\pm}(m_R, Q^2) \end{pmatrix} \cdot q_\gamma^{\mathrm{R}} |\vec{p}_\pi^{\,R}| q_\gamma |\vec{p}_\pi| \Gamma_{\mathrm{tot}}(m_R)\Gamma_\pi(m_R) \cdot \sqrt{s}\ \Gamma_\pi^{1/2}\Gamma_\gamma^{1/2} m_R^2 - s - i\sqrt{s}\ \Gamma_{\mathrm{t}} \tag{12}$$

with

$$\begin{aligned}
A_{l\pm}(m_R, Q^2) &= \mp F C_{\pi N}^I A_{1/2}(Q^2) \\
B_{l\pm}(m_R, Q^2) &= \pm F\sqrt{16(2j-1)(2j+3)} C_{\pi N}^I A_{3/2}(Q^2)
\end{aligned} \tag{13}$$

and

$$F = \sqrt{1\pi(2j+1) q_\gamma^R |\vec{p}_\pi^{\,R}| m_N m_R \Gamma_\pi \Gamma_{\mathrm{tot}}^{R\ 2}}.$$

$C_{\pi N}^I$ are the Clebsch-Gordan coefficients arising from the isospin coupling of pion and nucleon. The superscript 'R' denotes quantities taken at the resonance mass. Γ_{tot} and Γ_π are the energy dependent total decay width and the one-pion decay width of the resonance and are calculated according to [24]. Γ_γ is a parametrization of the q_γ-dependence of the γN width [25]. Eq.

(12) leads to the resonance cross section

$$\sigma_{\gamma^* N\to R\to\pi N} = \left(q_\gamma^R q_\gamma\right)^2 s\Gamma_\gamma\Gamma_{R\to\pi N}(s-m_R^2)^2 + s\Gamma_{\rm tot}^2 2m_N m_R\Gamma_{\rm tot}^R(|A_{1/2}|^2+|A_{3/2}|^2). \tag{14}$$

The photocoupling-helicity amplitudes $A_{1/2}$ and $A_{3/2}$ are functions of Q^2, for which we make the ansatz

$$\begin{aligned} A_{1/2}(Q^2) &= A_{1/2}(Q^2=0)\cdot f(Q^2) \\ A_{3/2}(Q^2) &= A_{3/2}(Q^2=0)\cdot g(Q^2). \end{aligned} \tag{15}$$

Since the amount of data points is rather limited, it is reasonable to keep the number of parameters as low as possible. Therefore we use the same form factor for both amplitudes, although the Q^2-dependence of these quantities is known to be different (e.g. [26]). Thus the form factors are fitted such that they reproduce the Q^2-dependence of the expression

$$|A_{1/2}|^2+|A_{3/2}|^2,$$

which equals the Q^2-dependence of the resonance cross section in eq. (14).

In our calculations the resonances $P_{33}(1232)$, $D_{13}(1520)$, $S_{11}(1535)$ and $F_{15}(1680)$ are taken into account in elementary $\gamma^* N$ interactions. For each of the partial waves, corresponding to the four resonances, we introduce a different form factor.

The background contributions to the partial-wave amplitudes were obtained in [11] by subtracting the resonance contributions (12) from the partial-wave amplitudes in [23]. To describe the Q^2-dependence, we introduce an additional fitting function $f^{1\pi}(Q^2)$. Then the cross section reads:

$$\begin{aligned} \sigma_T = \int d\Omega|\vec{p}_\pi|2q_\gamma\Bigg(\sum_{i=1}^{4}\Bigg|\sum_{l=0}^{3} H_i^{l,\rm res}(\vartheta,\sqrt{s},Q^2=0)\cdot f^l(Q^2) + \\ + H_i^{\rm bg}(\vartheta,\sqrt{s},Q^2=0)\cdot f^{1\pi}(Q^2)\Bigg|^2\Bigg). \end{aligned} \tag{16}$$

Here $H_i^{l,\rm res}$ stands for the resonant helicity amplitudes of partial wave l, i.e. for the contribution of the resonance with angular momentum l.

3.2 Eta Production

The cross section for eta production is parameterized under the assumption, that each elementary eta meson arises from the decay of an intermediate $S_{11}(1535)$. The cross section is then given according to eq. (14):

$$\sigma_{\gamma^* N\to\eta N} = \left(q_\gamma^R q_\gamma\right)^2 s\Gamma_\gamma\Gamma_{S_{11}(1535)\to\eta N}(s-m_{1535}^2)^2 + s\Gamma_{\text{tot}}^2 2m_N m_{1535}\Gamma_{\text{tot}}^R \times \\ \times |A_{1/2}(Q^2=0)\cdot f^{S_{11}(1535)}(Q^2)|^2, \tag{17}$$

where $f^{S_{11}(1535)}$ equals the form factor f^l in the last section for $l=0$.

3.3 Two-Pion Production

In [11] we have written the two-pion cross section $\gamma N\to\pi\pi N$ as an incoherent sum of a resonant and a background part. The resonant part is given in analogy to eq. (14). The difference between these contributions and the experimental data for $Q^2=0$ was treated as background. For finite Q^2, we introduce due to the absence of data in all two-pion channels another fitting function $f^{2\pi}$ and use the following expression for the background:

$$\sigma_{2\pi}^{\text{bg}}(Q^2) = \sigma_{2\pi}^{\text{exp}}(Q^2=0)\cdot f^{2\pi}(Q^2)^2 - \sum_R \sigma_{2\pi}^R(Q^2=0)\cdot f^R(Q^2)^2. \tag{18}$$

The parameters of $f^{2\pi}$ can be determined by fitting to the total cross section $\sigma(\gamma^* p\to X)$, since the two other main contributions $\gamma^* N\to\pi N$, $\gamma^* N\to\eta N$ are already known (cf. next section).

3.4 Formfactors

We now have to determine the four resonance form factors and the two functions $f^{1\pi}, f^{2\pi}$. We restrict ourselves to the range $Q^2\le 1.0$ GeV^2 and use the following ansatz:

$$f(Q^2) = \left(1+\left(Q^2 a\right)^b\right)^{-c}$$

with parameters a, b, c. Although the amount of experimental data is rather limited in the considered energy and Q^2 range, it is nevertheless possible to find a set of parameters with which most data can be described in a satisfactory way. For the fitting procedure we used data from the exclusive

channels $\gamma^* p \to \pi^0 p$, $\gamma^* p \to \pi^+ n$, $\gamma^* p \to p\eta$ and measurements of the helicity amplitudes $A_{1/2}, A_{3/2}$ for the resonances. The parameters are displayed in tab. 2. We stress here that we do not aim at a perfect extraction of resonance form factors, but only at a good description of the Q^2 dependence of (γ, meson) reactions on the nucleon.

We show the comparison of our calculations with data from the channels $\gamma^* p \to \pi^0 p$ for $Q^2 = 0.4, 0.6$ and 1.0 GeV^2 and $\gamma^* p \to \pi^+ n$ for $Q^2 = 0.35$ GeV^2 in fig. 2. In fig. 3 we compare with the Q^2-dependence of the transverse helicity amplitudes $|A_T| = (|A_{1/2}|^2 + |A_{3/2}|^2)^{1/2}$ of the resonances $D_{13}(1520)$ and $F_{15}(1680)$. For the $\Delta(1232)$, we show in fig. 3 a) the magnetic form factor [21]

$$|G_M^*(Q^2)|^2 = \left((Q^2 + m_\Delta^2 - m_N^2)^2 4m_N^2 + Q^2\right)^{-1} m_N 2\pi\alpha (m_\Delta^2 - m_N^2)(|A_{1/2}|^2 + |A_{3/2}|^2).$$

All these quatities do not depend on ε. The three different curves for the $\Delta(1232)$ and the $F_{15}(1680)$ in fig. 3 arise from the necessity of using different fit parameters for the three ε bins mentioned earlier. It can be seen that all three curves are consistent with the data. The cross section $\gamma^* p \to \eta p$ is dominated by the $S_{11}(1535)$ resonance and therefore reflects the Q^2-dependence of the helicity amplitude of this resonance (cf. eq. (17)).

The remaining functions $f^{1\pi}$ and $f^{2\pi}$ were determined by fitting the parameters to the total $\gamma^* p \to X$ cross section in [22] in the first and the second resonance region, respectively. This leads to an underestimation of the cross section in the third resonance region of up to 25μb. This difference has also been parametrized and treated as two-pion background. In fig. 4 we show the total cross section $\gamma^* p \to X$ for different values of Q^2 and $\varepsilon \geq 0.9$. For the two other ε bins, we obtain similar good agreement.

Since there are no data available for the different channels of the $\gamma^* n \to X$ cross section, we use the same form factors for both protons and neutrons.

4 The Processes $eA \to e'X$ and $\gamma A \to X$

In this section we are concerned with the process $eA \to e'X$ and the photoabsorption process $\gamma A \to X$, which has already been investigated in [10]. Using the elementary medium-modified cross sections on the nucleons derived in the last section, the differential cross section of this process can be

written in the form:

$$d\sigma_{eA\to e'X}dE'_e d\Omega = 4\int d^3r \int^{p_F} d^3p_N (2\pi)^3 \left(ZAd\sigma_{ep\to e'X}dE'_e d\Omega + NAd\sigma_{en\to e'X}dE'_e d\Omega\right), \tag{19}$$

with

$$d\sigma_{e(p,n)\to e'X}d\Omega_e dE'_e = d\sigma_{e(p,n)\to e'\pi N}d\Omega_e dE'_e + d\sigma_{e(p,n)\to e'\pi\pi N}d\Omega_e dE'_e + d\sigma_{e(p,n)\to e'\eta N}d\Omega_e dE'_e.$$

The Fermi momentum p_F is given by eq. (3). Note that the cross section has to be calculated in the rest frame of the nucleus, so we have to Lorentz-transform the cross sections on the nucleons appearing in (19), since they were derived in the rest frame of the nucleons. This can easily be done by using Lorentz invariance of the expression d^3p/E for the outgoing electron. Since the general expression for the differential cross section $d\sigma = |\mathcal{M}|^2 d\Phi/j$ (j: flux of incoming particles) involves the Lorentz invariant (matrix element)$^2\times$ phase space, the connection between the nucleon cross section in the rest frames of the nucleus (LAB) and the nucleon (R) is given by:

$$\left(d\sigma dE' d\Omega\right)_{LAB} = j^R j^{LAB} E'^{LAB} E'^R \left(d\sigma dE' d\Omega\right)_R .$$

In order to compare the cross sections of the processes $eA \to e'X$ and $\gamma A \to X$, one can define a cross section of the process $\gamma^* A \to X$ according to eq. (7) by

$$\sigma_{\gamma^* A\to X} = 1\Gamma d\sigma_{eA\to e'X}dE' d\Omega$$

with the flux factor Γ from eq. (8) [6].

We now turn to the influence of the different in-medium modifications to the cross section for different Q^2. In fig. 5 the case $Q^2 = 0$, which was discussed in detail in [10], is shown. The different curves show the different modifications which are turned on subsequently, as indicated in the legend. The elementary cross section without any modifications shows the three resonance regions. After turning on the Fermi motion of the nucleons the three resonance regions become smeared out, which causes the disappearance of the $F_{15}(1680)$. Pauli blocking leads to a slight decrease of the cross section in the Δ resonance region and a shift of the resonance maximum to larger energies. The inclusion of in-medium widths, i.e. Pauli-blocked one-pion widths and the additional collision width given by eq. (6) results in a shift of the Δ peak to smaller energies and a slight increase, which can be explained

by the fact that the ratio of in-medium and vacuum width of the Δ for energies up to the resonance mass roughly equals 1, whereas it increases quickly for energies above. The increase is due to the additional possible collision reactions of the Δ in the nucleus.

When we also consider that the Δ is less bound in the nucleus than the nucleons by using the Δ potential from eq. (5) (involving the momentum independent nucleon potential), the increasing Δ mass causes a shift of the first resonance region back to higher energies. The cross section again drops, since the Δ width increases with the mass.

After applying all medium modifications, one observes a discrepancy with the data from [4] in the Δ region which was already discussed in [10] and could be cured by the inclusion of a two-body absorption process $\gamma NN \to N\Delta$ [27].

At finite Q^2, there are additional scattering processes at energies below the Δ mass, which lead to the quasielastic peak. We do not consider these processes in our investigations. The quasielastic region is discussed in detail in [8], where the authors calculate the $eA \to e'X$ reaction within a Δ-hole model in the energy range up to the Δ resonance. The results on ^{12}C and ^{208}Pb show a good global agreement with the data.

As can be seen in figs. 5 and 6, the influence of the different in-medium modifications changes with increasing Q^2. First of all, we observe that the Fermi motion of the nucleons becomes more effective with increasing Q^2. The cms energy is given by

$$s = -Q^2 + m_N^2 + 2E_\gamma \sqrt{m_N^2 + \vec{p}_N^{\,2}} - 2\sqrt{Q^2 + E_\gamma^2}\, p_N^z. \tag{20}$$

The last term in this equation becomes more important for increasing Q^2, which causes the mentioned effect and leads to a broadening of the resonant contributions and a disappearance of the second resonance region already for $Q^2 \geq 0.2$ GeV^2. Pauli blocking is totally suppressed for $Q^2 \geq 0.2$ GeV^2 (both curves lie upon each other), because for increasing Q^2 the excitation of a certain resonance requires a larger momentum transfer, which leads to a rising nucleon momentum after decay. The consideration of in-medium widths results in a curve which lies below the one with Pauli blocking, different from the real photon case: The inclusion of the total in-medium width leads to a dropping of the one-pion contributions to the cross section because of the $1/\Gamma$ dependence of the resonant part (cf. eq. (14)). For $Q^2 = 0$ this decrease is compensated by the additional collision processes. For finite Q^2, one has

to take into account the different Q^2 dependencies of both contributions. In the collision part it is totally determined by the Δ form factor, whereas the one-pion contributions also involve the background processes, generating a smoother decrease for larger Q^2. Therefore the collision contributions become less important for increasing Q^2.

The Δ potential leads to a decrease of the cross section as before. The main observation is that the Fermi motion becomes the most important (though trivial) in-medium modification at large Q^2.

We now compare our calculations with data measured in the energy range of the the upper Δ resonance region. In fig. 7 we present our results for $\sigma(eA \to e'X)$ for different nuclei. The electron energies $E \approx 0.6 - 0.7$ GeV and the scattering angle $\vartheta = 60^\circ$ correspond to rather small values of Q^2 in the range of $0.05 - 0.2$ GeV^2. Since E and ϑ are fixed, Q^2 and ε vary as E_γ changes (see eqs. (9), (10)). In each plot we show the ranges of Q^2 and ε. We find excellent agreement with the experimental data in all cases.

In fig. 8 we show results on ^{12}C for different values of Q^2. Again, the comparison with the data shows very good agreement, although at $E = 1.5$ GeV we overestimate the data by about 15%.

So far we have seen that our model seems to be able to describe eA-reactions at least in the upper Δ resonance region. Additional measurements - especially in the higher resonance regions - is needed to finally determine whether this holds in the whole considered energy- and Q^2-region. The improved agreement in the Δ region compared to the case $Q^2 = 0$ without the inclusion of two-body absorption processes originates from the reduced de Broglie wavelength of the photon for finite Q^2. Therefore, the absorption process on single nucleons, as assumed in impulse approximation, is the dominating one.

4.1 Medium Modifications of the $D_{13}(1520)$

In fig. 5 one sees that for $Q^2 = 0$ the second resonance region is still visible, whereas the data clearly show a vanishing of any resonant structure. As discussed in [10] the structure in this region is not only caused by the excitation of the $D_{13}(1520)$, but also by the opening of the two-pion channel.

In the following we present different scenarios that might explain the disappearance of the $D_{13}(1520)$. The resonant contribution can be altered by using an enhanced in-medium width. This leads to a more smeared and re-

duced cross section. In [10] we have already proposed that the disappearance of the $D_{13}(1520)$ might be due to its strong coupling to the $N\rho$ channel and a medium modification of the rho meson. In [5] it has been shown within a resonance-hole model calculation for the spectral function of the rho meson that a self-consistent treatment of the $N\rho$ width of the D_{13} indeed gives a very large broadening. An enhancement of the $N\rho$ width at nuclear matter density by about a factor 10 was found which gives a total width at the pole mass of about 335 MeV. The use of this in-medium $N\rho$ width (including its full mass, momentum and density dependence) leads to the dashed curve in fig. 9. One sees that the description of the experimental data is considerably improved although for photon energies around 650 MeV some bump survives. This bump is caused by the strong mass dependence of the D_{13} width which is also present in the in-medium width.

The use of a momentum dependent N^* potential also leads to a smearing of the $D_{13}(1520)$, because the additional momentum dependent part in eq. (4) leads to a shift of the effective mass. For a $D_{13}(1520)$ produced with momenta around 800 MeV for which the nucleon potential almost vanishes, this shift amounts for $\Delta m^* \approx 50$ MeV. The broadening is due to the strong increase of the width with the mass. We observe an almost complete vanishing of the resonant structure but we still overestimate the experimental data slightly.

An adhoc collision width $\Gamma_{coll} = 300$ MeV as proposed by [29] shows quite good agreement with the data, but is hard to justify.

In [28] it has been shown that the disappearance of the D_{13} might be explained by an in-medium change of the two-pion production cross section which results mainly from a change in the interference structures of the different contributions due to conventional medium modifications. However, the model in [28] for the elementary $\gamma N \to N\pi\pi$ process is very simple and it remains to be seen if the effect also shows up in an more realistic calculation.

In [30] good agreement with the experimental data on the photoabsorption cross section has been achieved within a model calculation of the in-medium spectral function on the rho meson by using vector meson dominance. We note here that the D_{13} width has not been calculated self-consistently but the result of [5] has been adopted ignoring the mass and momentum dependence of this in-medium width, whereas we find a substantial influence in particular of the mass dependence of the width in our results, as shown above. Moreover, in [30] the model parameters have not been adjusted to exclusive observables like $\gamma N \to \pi N$, $\gamma N \to \pi\pi N$ as in

our calculation but only to the total γp cross section. Also the neglect of an isoscalar coupling of the photon to the nucleon in [30] might be questionable.

In fig. 9 we also show the different scenarios at $Q^2 = 0.4$ GeV^2. Again, one can see a dropping of the cross section in the second resonance region. The differences between the different scenarios are rather small, because the $D_{13}(1520)$ becomes already very broad due to Fermi motion.

5 Meson Production

5.1 Pion Production

We now investigate pion production cross sections by considering different medium modifications. For calculations involving virtual photons we use $\varepsilon \geq 0.9$. Besides Pauli blocking and Fermi motion of the nucleons we discuss different potentials and in-medium widths: For the Δ resonance, we use the $N\Delta \rightarrow NN$ and $N\Delta \rightarrow N\Delta$ collision and Pauli blocked one-pion widths from [10] ('standard' BUU treatment) for both the population and the final state interactions. We discuss the effects of a momentum dependent nucleon potential extracted from a 'medium' EOS and a momentum independent potential extracted from a 'hard' EOS (cf. sec. 2). The potentials are used for the nucleons and all resonances except for the Δ, for which we take the potential displayed in eq. (5).

In fig. 10 we compare both calculations for the reaction $\gamma^{*40}\mathrm{Ca} \rightarrow \pi^0 X$ for $Q^2 = 0$ and 0.4 GeV^2. The momentum independent nucleon potential leads to a slight shift of the cross section in the first resonance region to lower energies and a global enhancement at finite Q^2. This is so because at large nucleon momenta, the momentum dependent potential is larger than the momentum independent one. This leads to the different peak maximum energies seen in fig. 10. Furthermore, the width increases with the resonance mass, which leads to the relative dropping of the cross section obtained with the momentum dependent potential.

In figs. 11 and 12 we discuss the different treatments of the Δ in-medium width already addressed in sec. 2.1 and show our results for the cross section of the reaction $\gamma^{*40}\mathrm{Ca} \rightarrow \pi^0 X$ for different Q^2 involving the three collision widths. The respective curves are labelled by 'BUU', 'spreading potential' and 'Δ-hole'. All calculations have been performed by using the momentum dependent nucleon potential mentioned above. In addition, we show

a calculation involving the 'spreading potential' width and the momentum independent potential. The use of the Δ-hole and spreading potential widths reduce the cross sections by about 30% of the BUU-width calculation, with the spreading potential curve lying slightly below the Δ-hole curve. This can be understood, because the BUU width leads to a smaller total Δ in-medium width and thus to larger cross sections $\gamma^* N \to \Delta \to X$ (cf. eq. (14)). The use of the momentum independent potential leads to the effects discussed earlier in connection with in fig. 10.

In fig. 13 we show the cross sections $\gamma^* A \to \pi^0 X$ on Pb and C, using the spreading potential and Δ-hole width. For $Q^2 = 0$ we show the data from [31]. We see that the usage of these Δ widths lead to a satisfying description of the data.

In figs. 14 and 15 we show the momentum differential cross section $d\sigma(\gamma^{*40}\mathrm{Ca} \to \pi^0 X)/dp_\pi/A$ for different Q^2. We consider the energies $\sqrt{s} = 1.23$ GeV, where the Δ is excited mainly in the $\gamma^* N$ reactions and $\sqrt{s} = 1.44$ GeV, where the Δ excitation takes place through produced pions in the final state interactions. Here $\sqrt{s} = (-Q^2 + m_N^2 + 2E_\gamma m_N)^{1/2}$ denotes the cms energy involving a nucleon at rest. We compare different calculations using the three Δ collision widths and also show the elementary pion spectra obtained by suppressing all final state interactions (curve 'w/o π fsi'). The distributions are peaked at momenta around $p_\pi = 0.2$ GeV for all Q^2 and both energies. The peak is due to the strong absorption of the pions by the nucleons for momenta $p_\pi \gtrsim 300$ MeV. For larger Q^2, the spectra become more smeared out compared to $Q^2 = 0$ due to the fact that more pions with larger momenta are produced in the elementary $\gamma^* N$ reactions. We observe significant differences between the three curves in the peak area whereas at large momenta the differences become negligible.

The curves involving the spreading potential and Δ-hole collision width show a satisfying agreement with the data for $Q^2 = 0$ from the TAPS collaboration [32, 33], which holds for both the shape and the magnitude of the spectra.

5.1.1 Effects of Medium Modifications of the $D_{13}(1520)$ Resonance

In fig. 16 we discuss the influence of the medium modifications of the $D_{13}(1520)$ already considered in the last section on the reaction $\gamma^{*40}\mathrm{Ca} \to \pi^0 X$ for $Q^2 = 0$ and $Q^2 = 0.4$ GeV^2. The curve labelled with 'momentum independent U_N' refers to a calculation using the Δ-hole collision width

and the Δ potential from eq. (5) with the momentum independent nucleon potential. The additional use of a 300 MeV collision width for both population and decay of the $D_{13}(1520)$ clearly leads to a strong reduction of the cross section in the second resonance region. Using the modified $N\rho$ decay width described in the last section instead, we observe a reduction of the cross section. Now rho mesons are produced at a higher rate, but most of them contribute to pion production via direct decay or excitation of an intermediate resonance with subsequent pion decay. A calculation using the momentum dependent nucleon potential instead of $D_{13}(1520)$ modifications also results in a dropping of the cross section. In the second resonance region the additional momentum dependent term leads already for $Q^2 = 0$ to a significantly larger effective resonance mass, which influences the cross section through the changed total width.

In figs. 17 and 18 we show our results for the cross sections $\gamma^{*40}\mathrm{Ca} \to \pi^+\pi^- X$ and $\gamma^{*40}\mathrm{Ca} \to \pi^0\pi^0 X$. For $Q^2 = 0$ we see a strong increase of the cross sections at about 0.5 GeV, whereas at energies above 0.7 GeV it varies only weakly. For $Q^2 = 0.4$ GeV^2 this behaviour is washed out. The different medium modifications of the $D_{13}(1520)$ lead to very similar results.

5.2 Eta Production

The investigation of eta production cross sections gives insight into the ηN dynamics and the behaviour of the $S_{11}(1535)$ in nuclear matter, since all primarily produced etas stem from the excitation of a $S_{11}(1535)$ resonance. As we have shown in [11], the cross sections are dominated by the primary etas, the contributions from secondary processes such as $\pi N \to \eta N$ are negligible. In fig. 19 we show the total cross section of the reaction $\gamma^{*40}\mathrm{Ca} \to \eta X$, where one observes a broadening and dropping of the cross section with increasing Q^2. For $Q^2 = 0$ we obtain good agreement with the data from [34] (see also [11], where the agreement was slightly better; the difference between the two calculations is due to systematic uncertainties in the transport calculation, such as initialization and resonance properties).

In fig. 20 we show our results for the energy differential cross section $d\sigma(\gamma^{*40}\mathrm{Ca} \to \eta X)/dT_\eta/A$ for $\sqrt{s} = 1.54$ GeV and different Q^2. The data from [34] for $Q^2 = 0$ are also shown. The calculation labelled by 'usual xsection' involved the momentum independent nucleon potential. The shift of the calculated spectrum to higher eta energies at $Q^2 = 0$ compared to the data was discussed in [35]. There it was shown, that the structure of the

spectra could be explained by using the energy independent cross sections $\sigma(\eta N \to \eta N) = 20$ mb and $\sigma(\eta N \to \pi N) = 30$ mb for the final state interactions; for higher eta kinetic energies these values are larger than those one obtains from an interaction through the $S_{11}(1535)$ alone. The corresponding curves (labelled by 'constant xsection') are also shown. The spectra are reduced at larger eta kinetic energies, because in this range the constant inelastic cross section exceeds the cross section used in the usual resonance model, which leads to a relative loss of etas. Also shown are the eta spectra obtained by suppressing all final state interactions (curve 'w/o η fsi').

For increasing Q^2 we observe that the maximum of the spectrum moves towards higher kinetic energies. A investigation at different $\sqrt{s}$ leads to the same result. In the pion spectra in figs. 14 and 15 such a shift of the distributions was not observed. This behaviour can be explained, if one recalls that the detected eta mesons do not undergo final state interactions at such a degree as the pions. Therefore, the eta spectrum is mainly due to the emission spectrum of the $S_{11}(1535)$. This is supported by the fact that the curves calculated without final state interactions show the same structure as the physical eta spectra. For large Q^2 the momentum transfer increases and so does the average momentum of the initially produced $S_{11}(1535)$ and its decay products, which shifts the eta spectrum. The measurement of eta electroproduction may therefore clarify whether the $\eta N - S_{11}(1535)$ dynamics is treated correctly in our model.

6 Summary

We have presented calculations of inclusive electroproduction and photoproduction processes on nuclei in the resonance region within a model that can take coupled channel effects in the final state interactions into account.

The cross section for the $\gamma^* N$ processes have been parametrized by using the γN cross sections of the respective channels to describe the energy dependence and introducing form factors for the Q^2-dependence. These form factors have been obtained by fits to data in different channels.

In addition to [10], we have discussed modifications of the photoabsorption cross section on nuclei for the $D_{13}(1520)$, which led to a better description of the data in the second resonance region. The results for $\gamma^* A \to X$ processes at finite Q^2 are found to be strongly dominated by the Fermi motion of the nucleons which leads to a disappearance of the second resonance

region for $Q^2 \geq 0.2$ GeV^2. Other medium modifications like Pauli blocking, in-medium widths and Δ potential do not show much influence at large Q^2. The comparison with data in the Δ region above the Δ peak has shown very good agreement for several kinematics of the scattered electrons.

Turning to meson production on nuclei, we first discussed several treatments of the Δ width, originating from the phenomenological spreading potential and calculations of the Δ self energy, which included the absorption of Δs on more than one nucleon. The comparison with the approach in [11] has shown smaller total and momentum-differential cross sections. The discussion of the momentum-differential π^0-cross section showed a peak at pion momenta around 0.2 GeV, remaining there for increasing Q^2. The energy differential cross section for eta production has shown a distribution moving towards higher energies for increasing Q^2.

Additional measurements of meson electroproduction on nuclei are inevitable, because this could answer different questions, e.g. whether the Q^2-dependences of the elementary gamma-nucleon processes are chosen correctly; also aspects concerning the resonance and meson dynamics in nuclei could be clarified.

References

[1] C.M. Ko, V. Koch and G.Q. Li, Ann. Rev. Nucl. Part. Sci. 47 (1997), 505

[2] G. Agakichiev et al., Phys. Rev. Lett. 75 (1995), 1272

[3] M.A. Mazzoni, Nucl. Phys. A 566 (1994), 95c; M. Masera, Nucl. Phys. A 590 (1995), 93c

[4] N. Bianchi et al., Phys. Rev. C54 (1996), 1688

[5] W. Peters, M. Post, H. Lenske, S. Leupold and U. Mosel, Nucl. Phys. A632 (1998), 109

[6] P. Barreau et al., Nucl. Phys. A402 (1983), 515

[7] R.M. Sealock et al., Phys. Rev. Lett. 62 (1989), 1350

[8] A. Gil, J. Nieves and E. Oset, Nucl. Phys. A627 (1997), 543

[9] A. Gil, J. Nieves and E. Oset, Nucl. Phys. A627 (1997), 599

[10] M. Effenberger, A. Hombach, S. Teis and U. Mosel, Nucl. Phys. A613 (1997), 353

[11] M. Effenberger, A. Hombach, S. Teis and U. Mosel, Nucl. Phys. A614 (1997), 501

[12] M. Effenberger, E.L. Bratkovskaya and U. Mosel, nucl-th/9903026

[13] S. Teis et al., Z. Phys. A356 (1997), 421

[14] A. Hombach, W. Cassing, S. Teis and U. Mosel, nucl-th/9812050, Eur. Phys. J. A, in press

[15] M. Effenberger, E.L. Bratkovskaya, W. Cassing and U. Mosel, nucl-th/9901039

[16] B. Anderson, G. Gustafson and Hong Pi, Z. Phys. C57 (1993), 485

[17] W. Cassing, V. Metag, U. Mosel and K. Niita, Phys. Rep. 188 (1990), 363

[18] M. Hirata, J.H. Koch, F. Lenz and E.J. Moniz, Ann. Phys. 120 (1979), 205

[19] T. Ericson and W. Weise, Pions and Nuclei, Clarendon Press, Oxford 1988

[20] E. Oset and L.L Salcedo, Nucl. Phys. A468 (1987), 631

[21] P. Stoler, Phys. Rep. 226 (1993), 104

[22] F.W. Brasse et al., Nucl. Phys. B110 (1976), 413

[23] R.A. Arndt, R.L. Workman, Z. Li and L.D. Roper, Phys. Rev. C42 (1990), 1853

[24] D.M. Manley and E.M. Saleski, Phys. Rev. D45 (1992), 4002

[25] R.L. Walker, Phys. Rev. 182 (1969), 1729

[26] M. Warns, H. Schröder, W. Pfeil and H. Rollnik, Z. Phys. C45 (1990), 627

[27] R.C. Carrasco and E. Oset, Nucl. Phys. A536 (1992), 445

[28] M. Hirata, K. Ochi and T. Takaki, Phys.Rev.Lett. 80 (1998), 5068

[29] L.A. Kondratyuk, M.I. Krivoruchenko, N. Bianchi, E. De Sanctis and V. Muccifora, Nucl. Phys. A579 (1994), 453

[30] R. Rapp, M. Urban, M. Buballa and J. Wambach, Phys. Lett. B417 (1998), 1; R. Rapp, nucl-th/9804065

[31] J. Arends et al., Nucl. Phys. A454 (1986), 579

[32] B. Krusche, private communication and to be published

[33] B. Krusche, Acta Phys. Pol. B29 (1998), 3335

[34] M.E. Röbig-Landau et al., Phys. Lett.B373 (1996), 45

[35] M. Effenberger and A. Sibirtsev, Nucl. Phys. A632 (1998), 99

[36] W.J. Shuttleworth et al., Nucl. Phys. B45 (1972), 428

[37] R. Siddle et al., Nucl. Phys. 35 (1971), 93

[38] J.C. Alder et al., Nucl. Phys. B105 (1976), 253

[39] A. Latham et al., Nucl. Phys. B189 (1981), 1

[40] S. Galster et al., Phys. Rev. D5 (1972), 519

[41] F.W. Brasse et al., Nucl. Phys. B139 (1978), 37

[42] T.A. Armstrong et al., Phys. Rev. D5 (1972), 1640

[43] Baldini, Flamino, Moorhead and Morrison, Landolt-Börnstein, Band 12, Springer Verlag, Berlin 1987

[44] Z.E. Meziani et al., Phys. Rev. Lett. 54 (1985), 1233

[45] A. Zghiche et al., Nucl. Phys. A572 (1994), 513

[46] E. Amaldi, Pion-Electroproduction, Springer Tracts in modern physics 83, Berlin 1979

[47] S. Stein et al., Phys. Rev. D12 (1975), 1884

[48] B. Krusche et al., Phys. Rev. Lett. 74 (1995), 3736

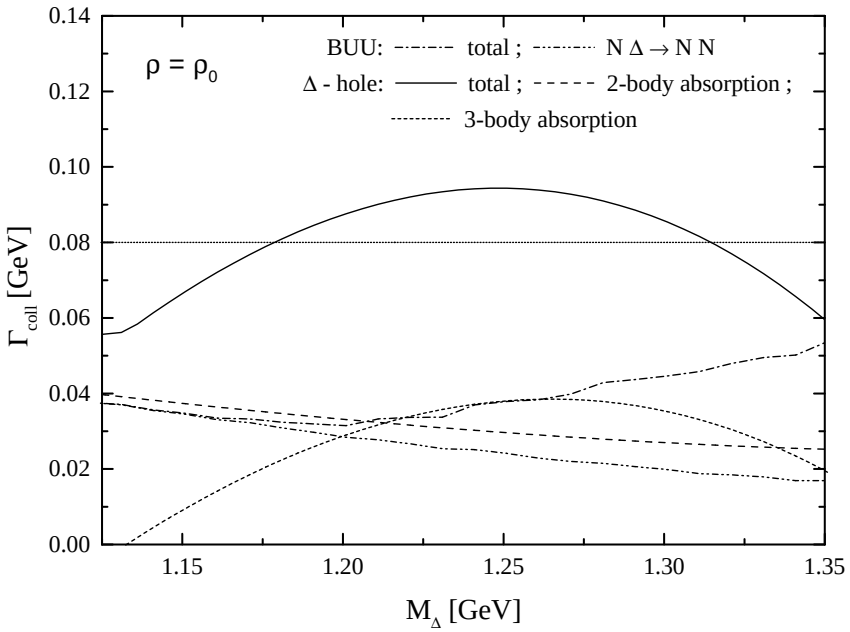

Figure 1: Comparison of the different Δ in-medium widths. The curves labelled with 'BUU' correspond to the treatment in [10], the curves labelled with 'Δ-hole' to that of [20]. The quasielastic contributions are not displayed, but included in the total widths. Also shown is the constant collision width extracted from the spreading potential.

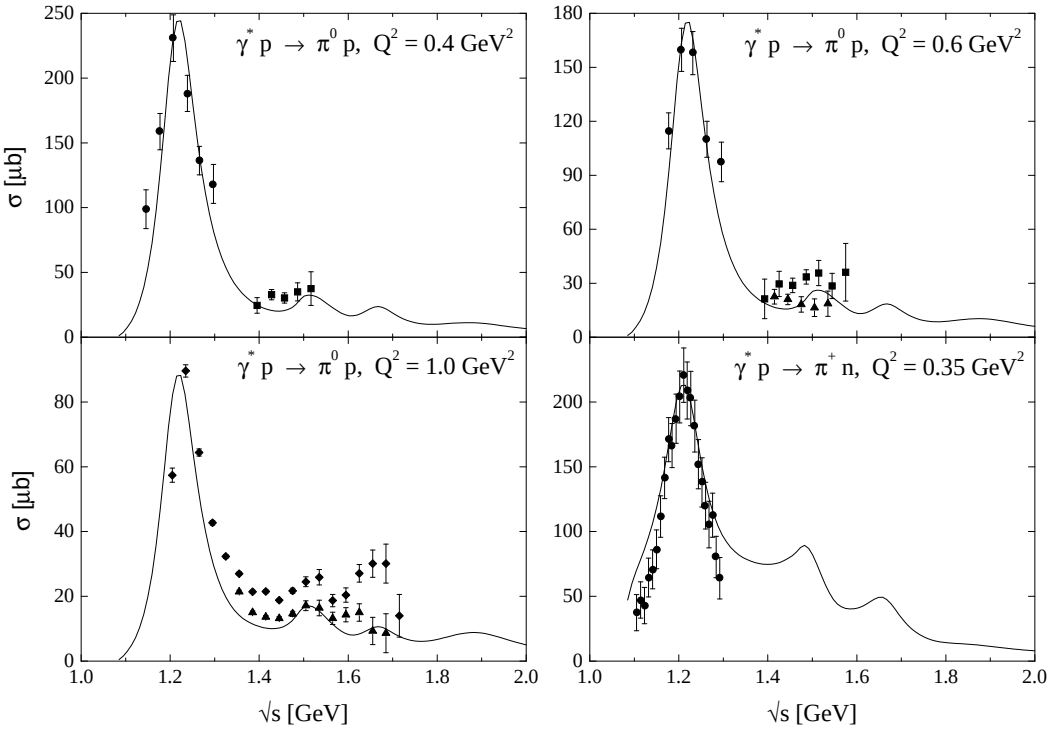

Figure 2: Comparison between pion electroproduction data and our calculations for different values of Q^2. a) - c): Cross sections of the reaction $\gamma^* p \to \pi^0 p$ reaction for different Q^2. The data are from [36] (circles), [37] (squares), [38] (triangles) and [39] (diamonds). d): Cross section of the reaction $\gamma^* p \to \pi^+ n$-cross section. The data are from [40].

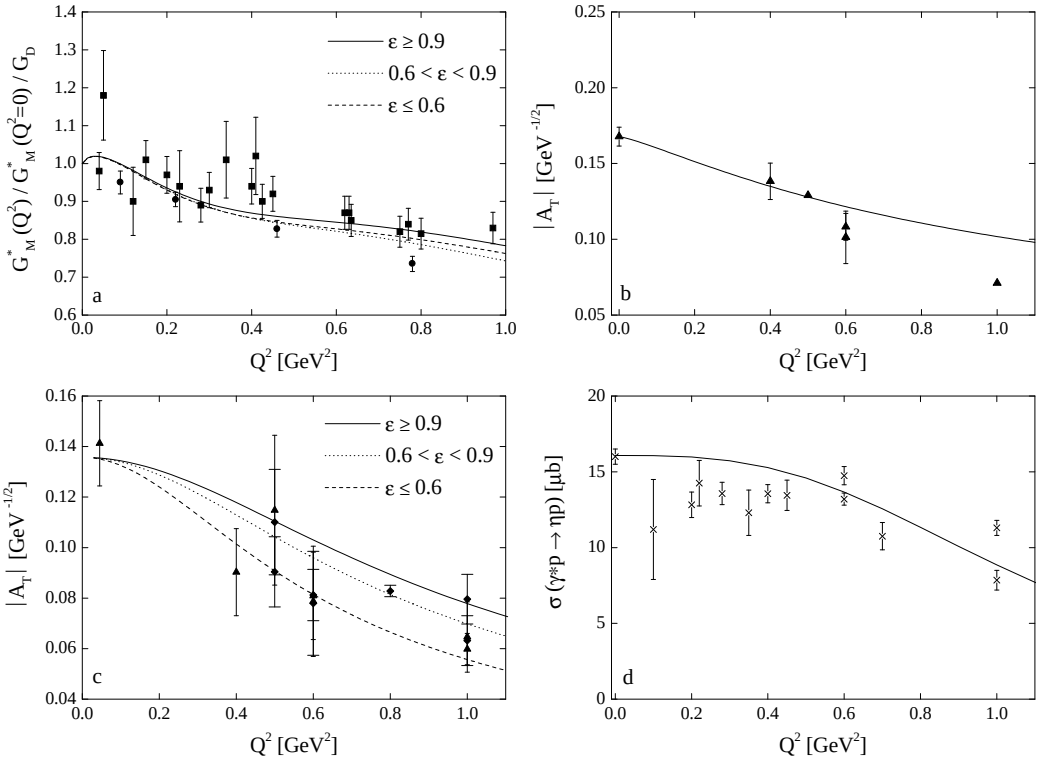

Figure 3: a) Magnetic form factor of the $\Delta(1232)$. The curves correspond to different ε-bins, as indicated in the legend. The data are from [46] (squares) and [47] (circles). b) Transverse helicity amplitude $|A_T|$ for the $N(1520)$. The data are from [26]. c) Transverse helicity amplitude $|A_T|$ for the $N(1680)$. The curves correspond to the ε-bins shown in the legend. The data are from [26] (triangles) and [21] (diamonds). d) Cross section of the reaction $\gamma^* p \to \eta p$ for $\sqrt{s} = 1.535$ GeV. The data are from [41]. The data point for $Q^2 = 0$ is from [48]

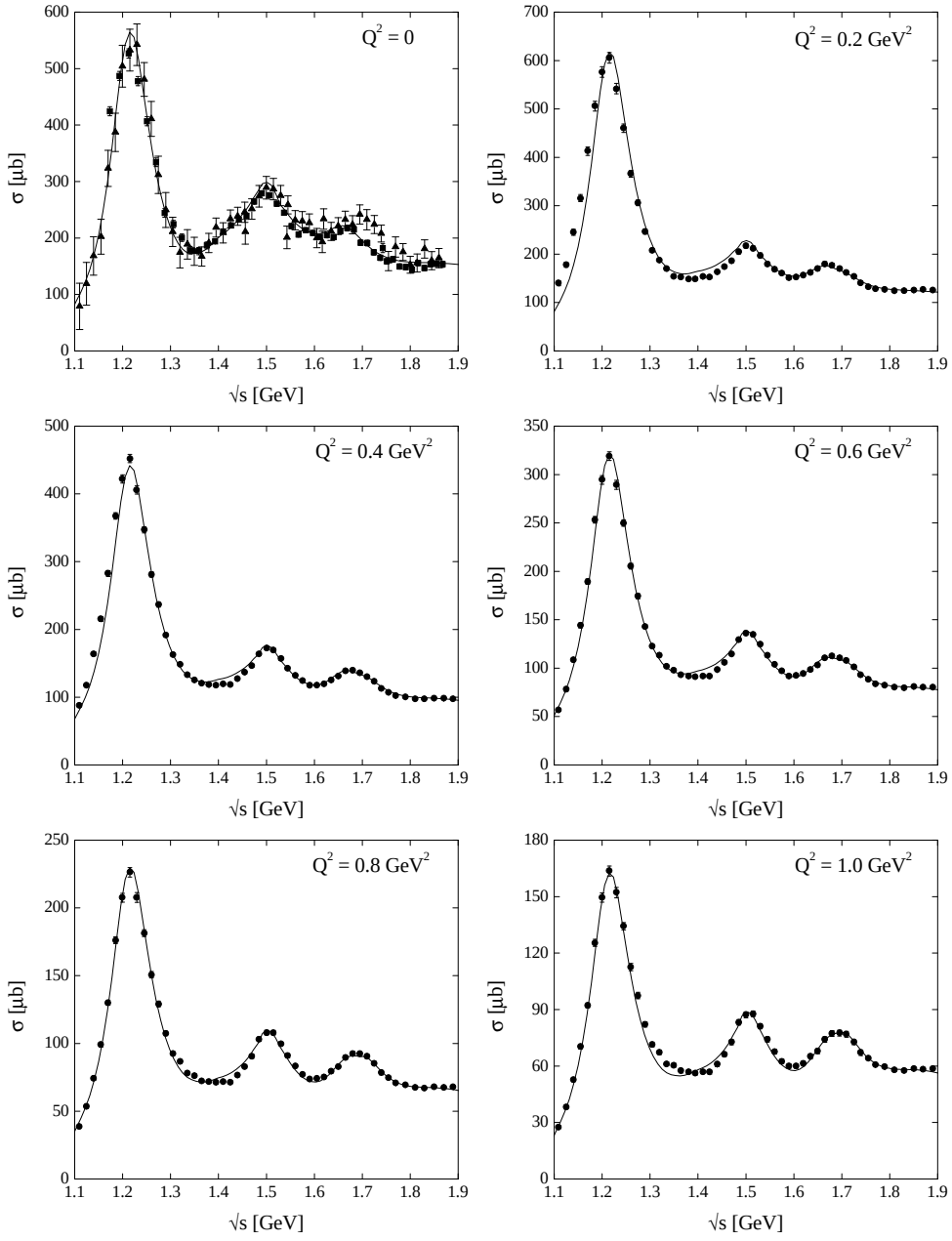

Figure 4: Total cross section of the reaction $\gamma^* p \to X$ for $\varepsilon \geq 0.9$ and different Q^2. For $Q^2 = 0$ the data are from [42] (squares) and [43] (triangles). For finite Q^2 the data are from [22].

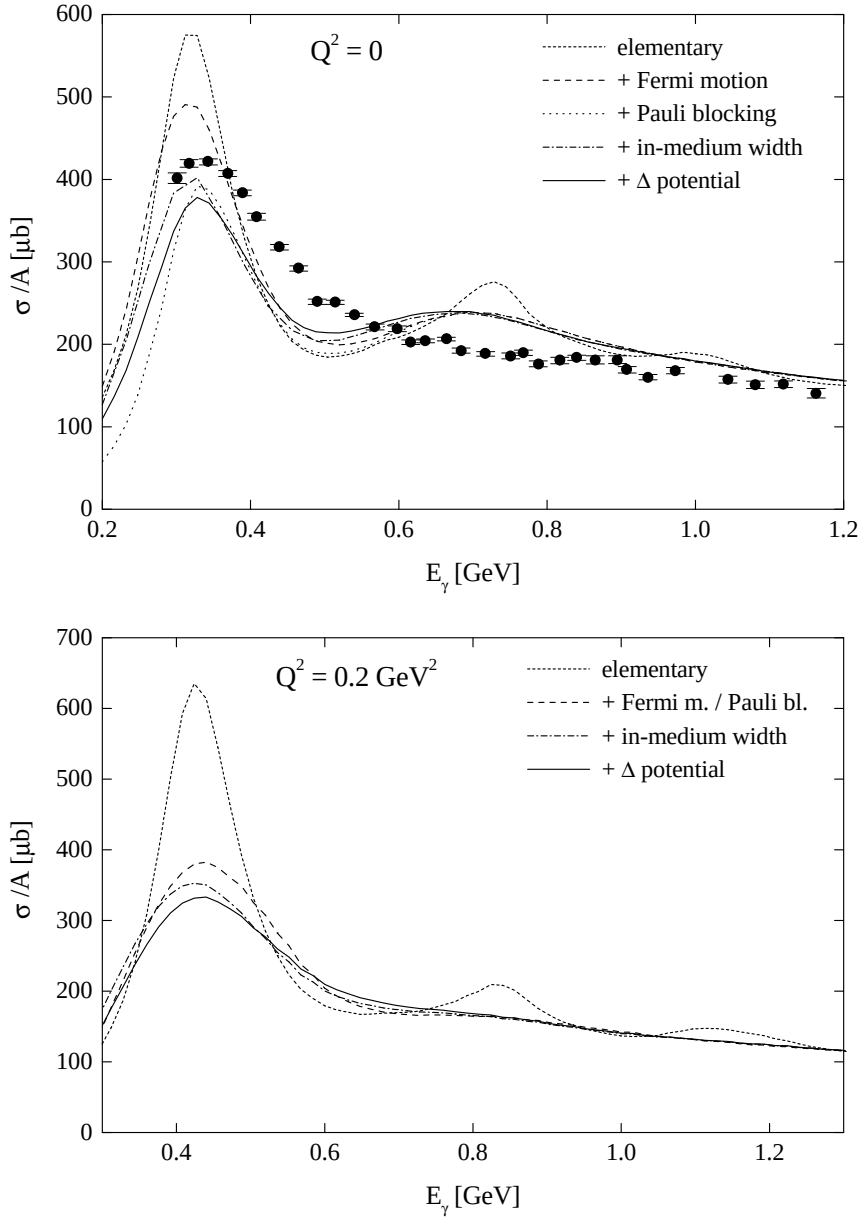

Figure 5: Influence of different in-medium modifications on the cross section of the reaction $\gamma^{*40}\mathrm{Ca} \to X$ for different Q^2 and $\varepsilon \geq 0.9$. The different modifications are switched on subsequently. All contributions due to quasieleastic scattering have not been taken into account. The data are from [4] and were obtained from an average over different nuclei.

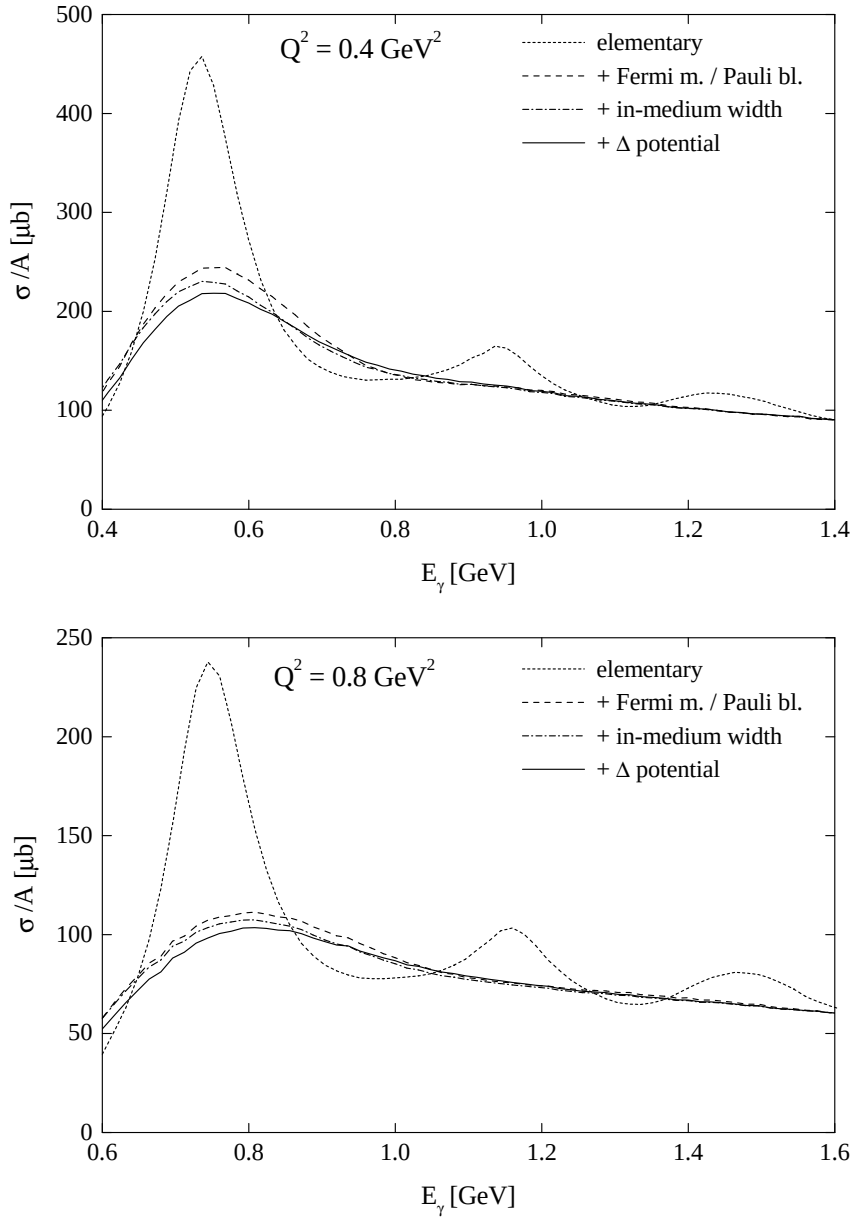

Figure 6: Influence of different in medium modifications on the cross section of the reaction $\gamma^{*40}\mathrm{Ca} \to X$ for different Q^2 and $\varepsilon \geq 0.9$. The different modifications are switched on subsequently. All contributions due to quasielastic scattering have not been taken into account.

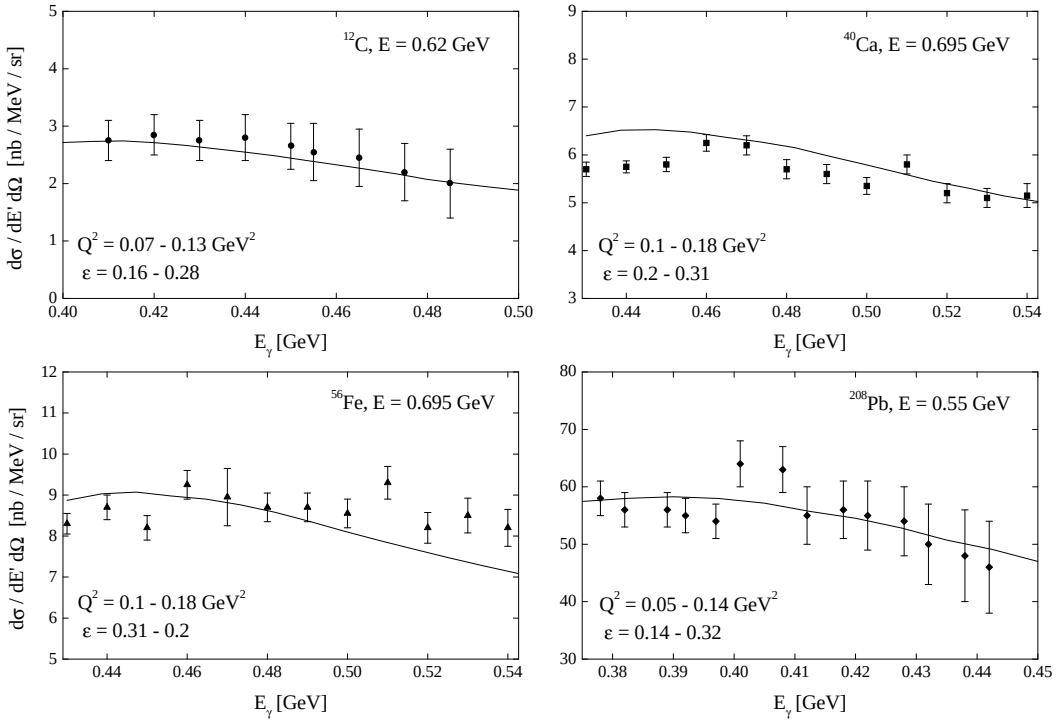

Figure 7: Cross section of the reaction $eA \to e'X$ measured at $\vartheta = 60°$ on different nuclei for different initial electron energies. The considered energy range corresponds to the upper Δ region. The Q^2 and ε ranges are shown in the plots. The data are from [6] (circles), [44] (squares and triangles) and [45] (diamonds).

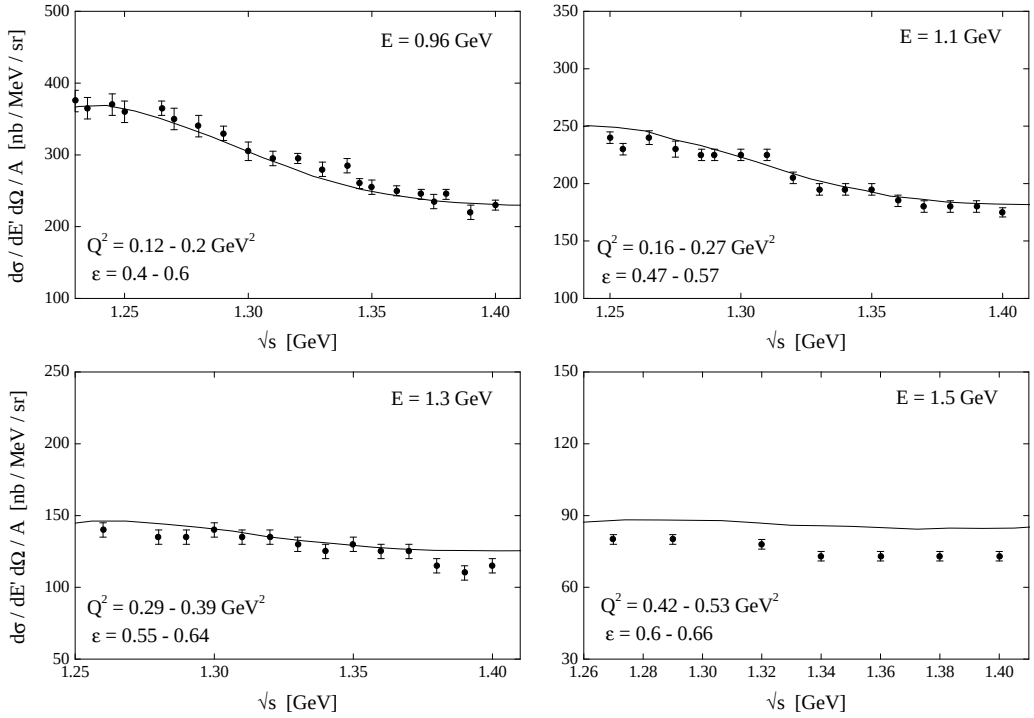

Figure 8: Cross section of the reaction $e^{12}\mathrm{C} \to e'X$ measured at $\vartheta = 37.5°$ for different initial electron energies. The energy range corresponds to the upper Δ region. The Q^2 and ε ranges are shown in the plots. The data are from [7].

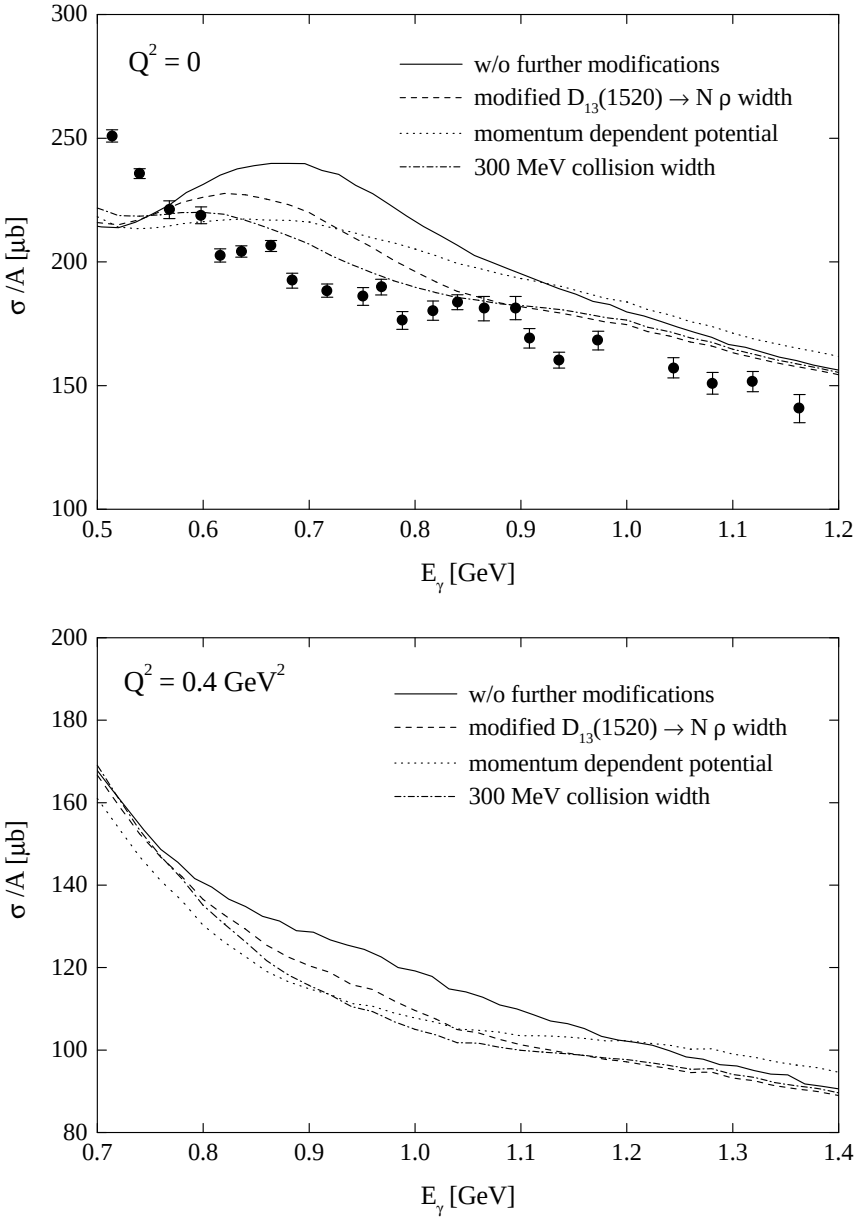

Figure 9: Modifications of the second resonance region for the $\gamma^{*40}\mathrm{Ca} \to X$-cross section. The data are from [4].

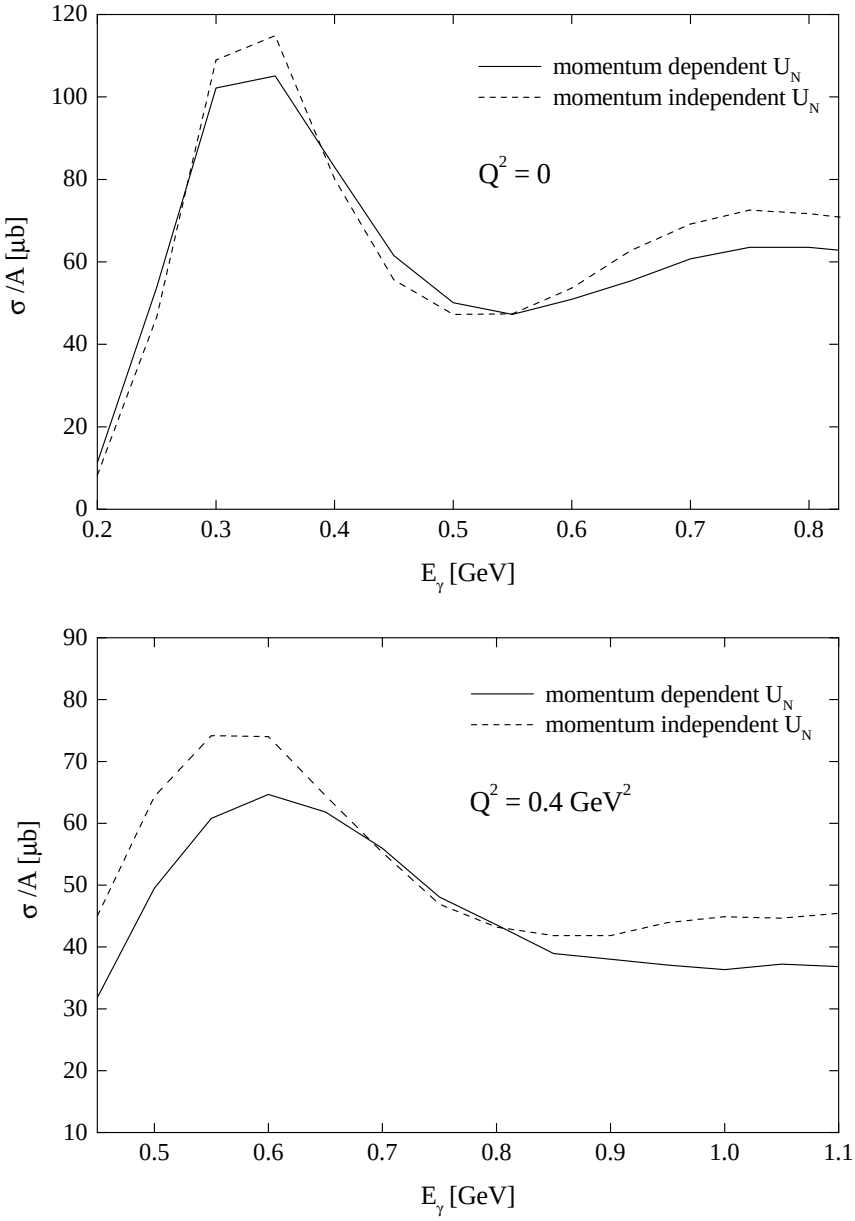

Figure 10: Total cross section of the reaction $\gamma^{*40}\mathrm{Ca} \to \pi^0 X$ for $Q^2 = 0$ and 0.4 GeV^2. The different curves correspond to the use of momentum-dependent and -independent nucleon potentials.

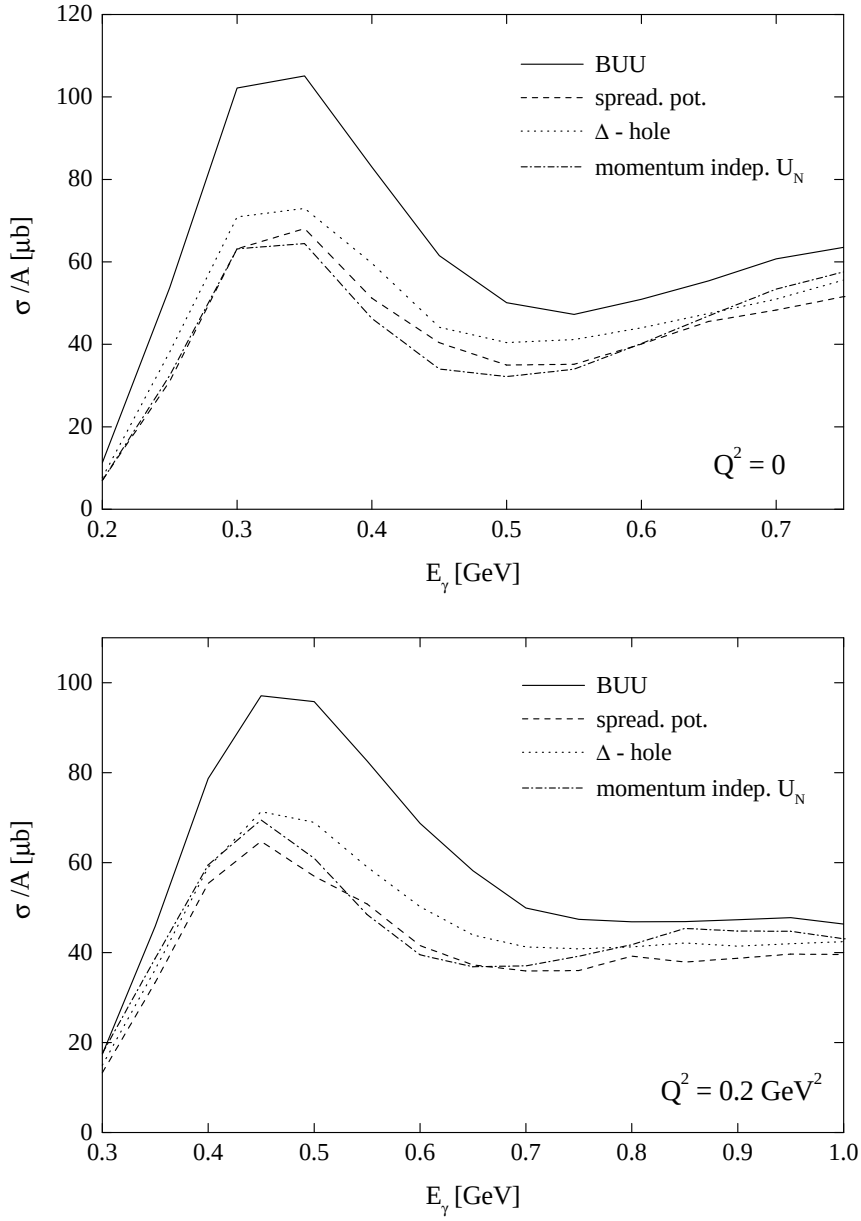

Figure 11: Total cross section of the reaction $\gamma^{*40}\mathrm{Ca} \to \pi^0 X$ for different Q^2.

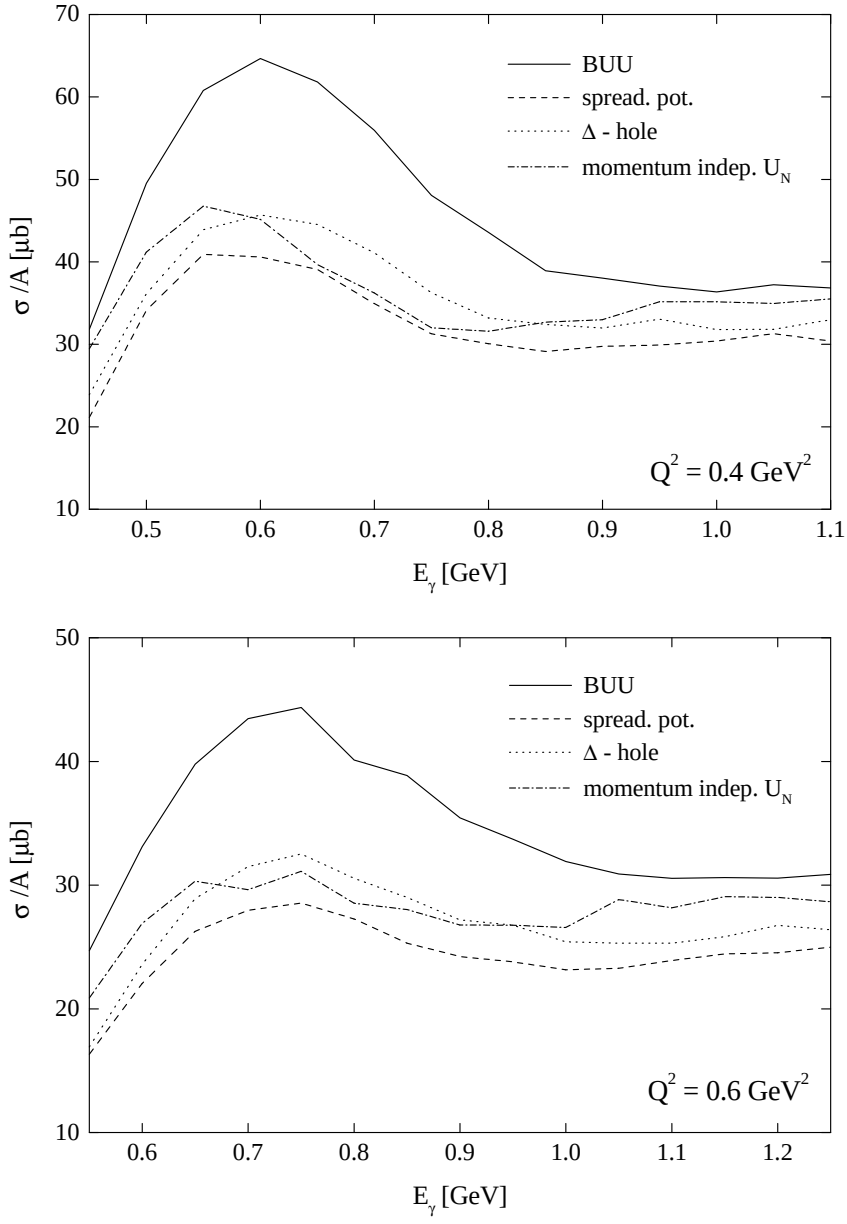

Figure 12: Total cross section of the reaction $\gamma^{*40}\mathrm{Ca} \to \pi^0 X$ for different Q^2. The medium modifications are explained in the text.

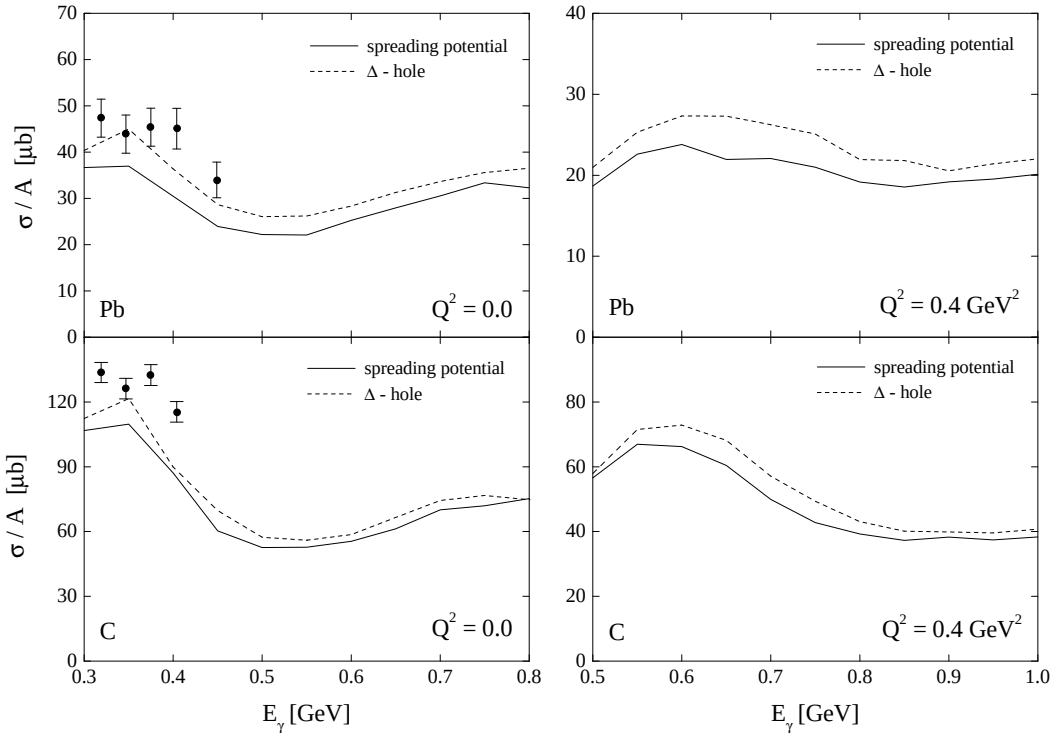

Figure 13: Total cross section of the reaction $\gamma^* A \to \pi^0 X$ on Pb and C for $Q^2 = 0$ and 0.4 GeV^2. The curves have been calculated using the spreading potential and Δ-hole collision width. The data are from [31].

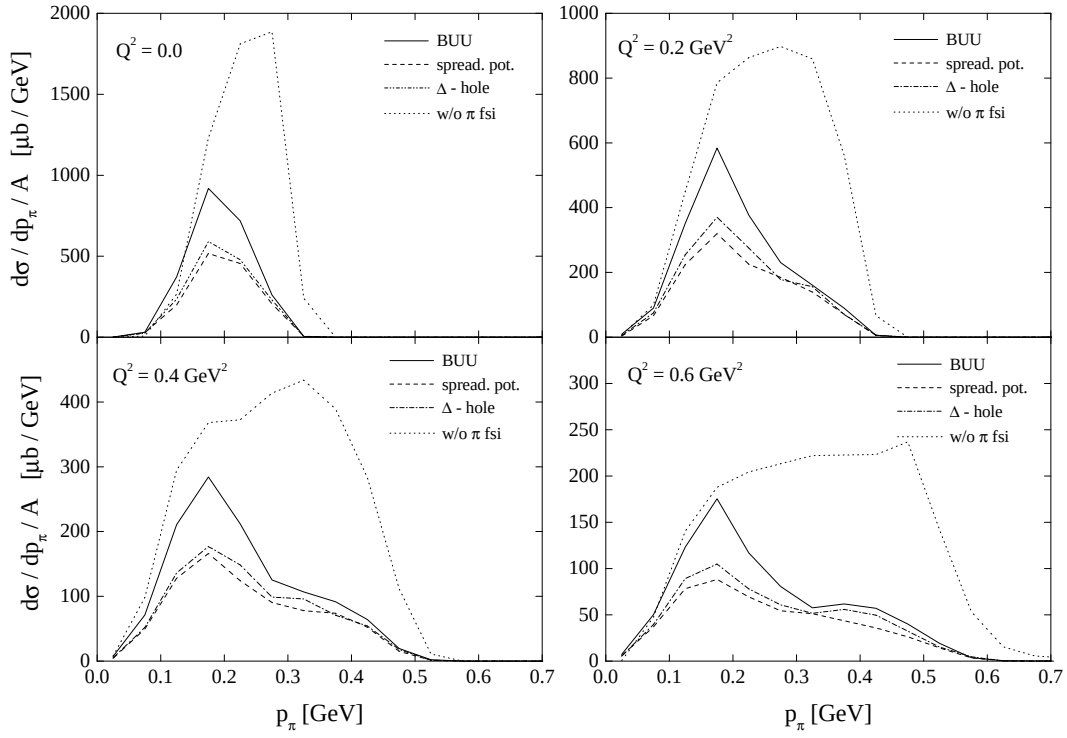

Figure 14: Momentum differential cross section of the reaction $\gamma^{*40}\mathrm{Ca} \rightarrow \pi^0 X$ for different Q^2 and $\sqrt{s} = (-Q^2 + m_N^2 + 2E_\gamma m_N)^{1/2} = 1.23$ GeV. The medium modifications are explained in the text.

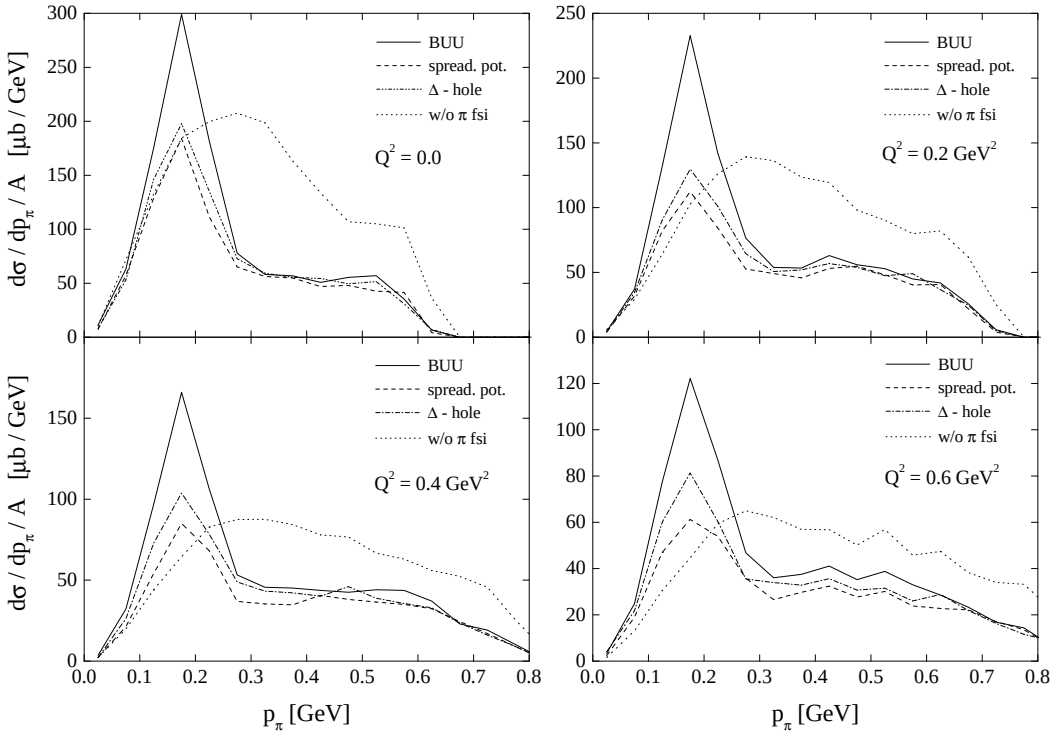

Figure 15: Momentum differential cross section of the reaction $\gamma^{*40}\mathrm{Ca} \rightarrow \pi^0 X$ for different Q^2 and $\sqrt{s} = (-Q^2 + m_N^2 + 2E_\gamma m_N)^{1/2} = 1.44$ GeV. The medium modifications are explained in the text.

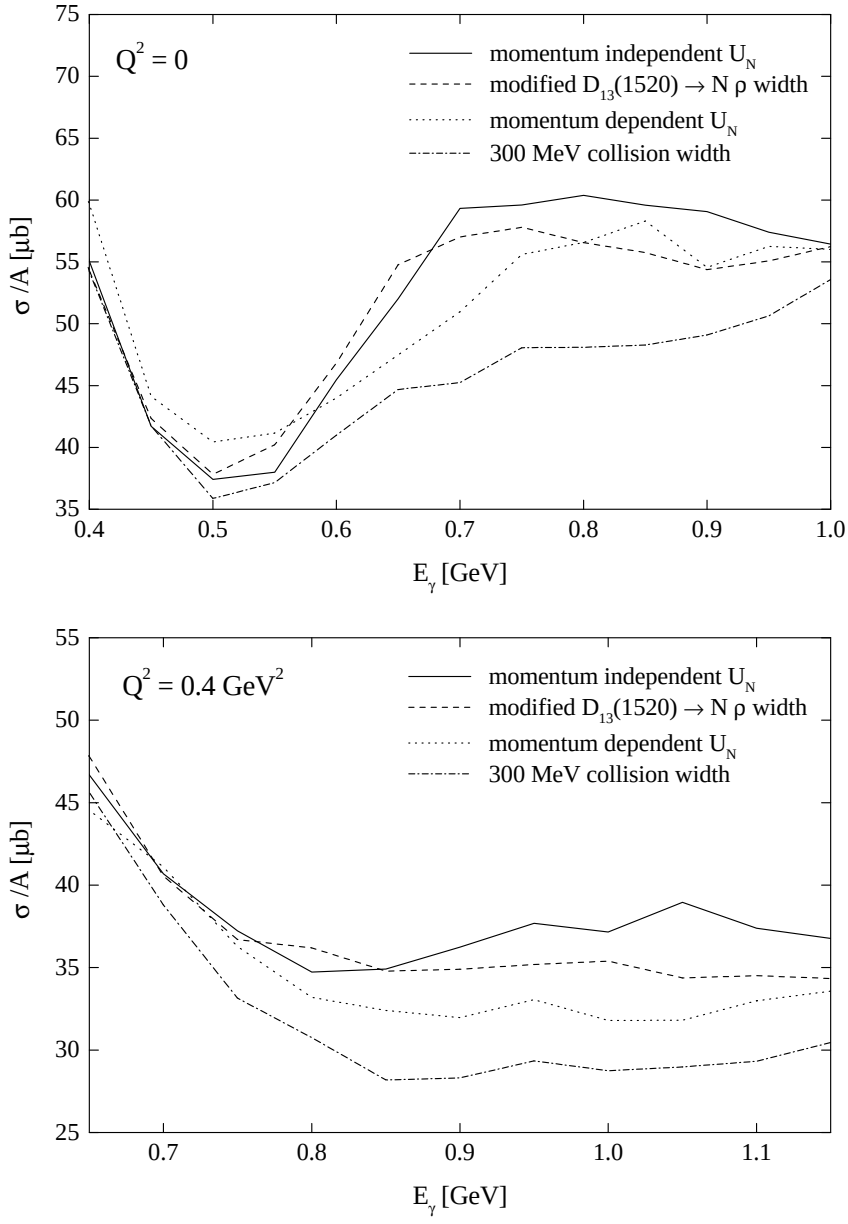

Figure 16: Modifications to the cross section of the reaction $\gamma^{*40}\mathrm{Ca} \to \pi^0 X$ in the second resonance region for $Q^2 = 0$ and 0.4 GeV^2. For explanations see text.

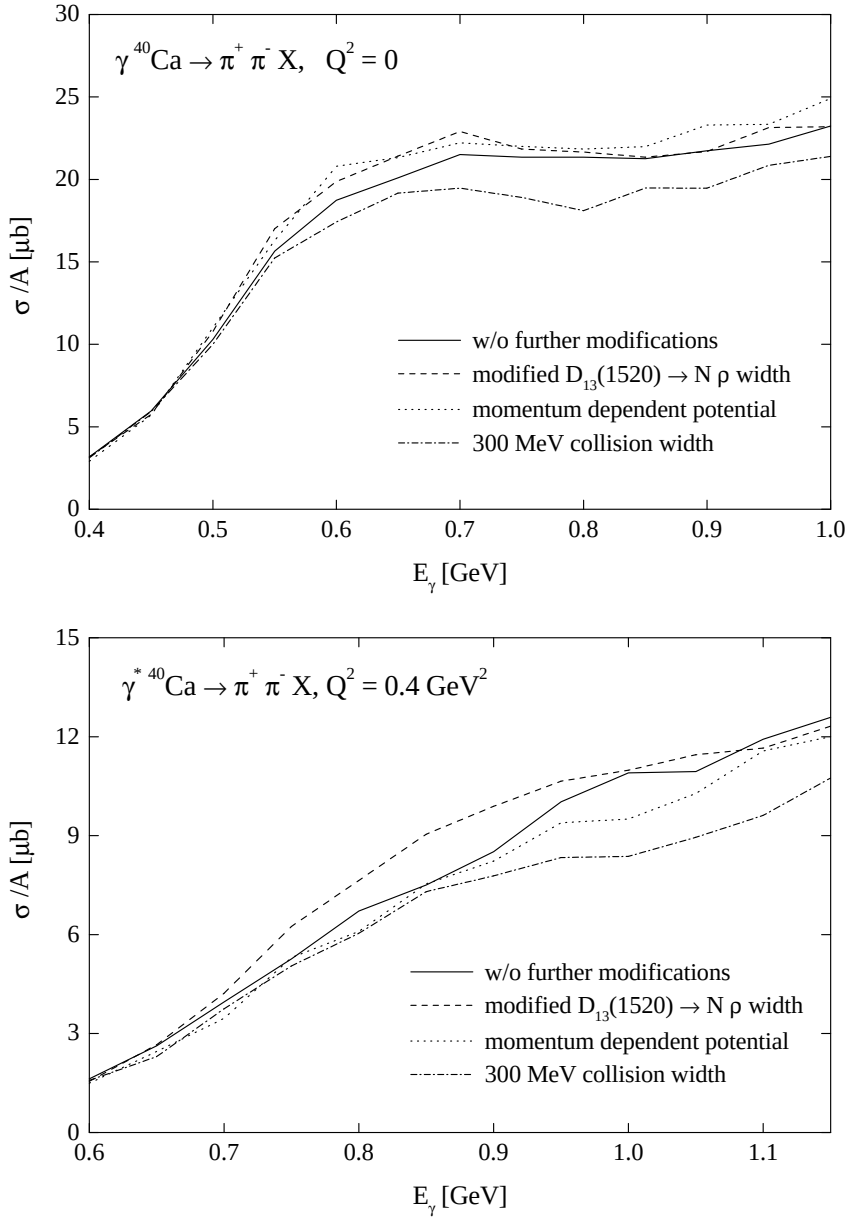

Figure 17: Cross section of the reaction $\gamma^{*40}\mathrm{Ca} \to \pi^+\pi^- X$ for different Q^2. The medium modifications are explained in the text.

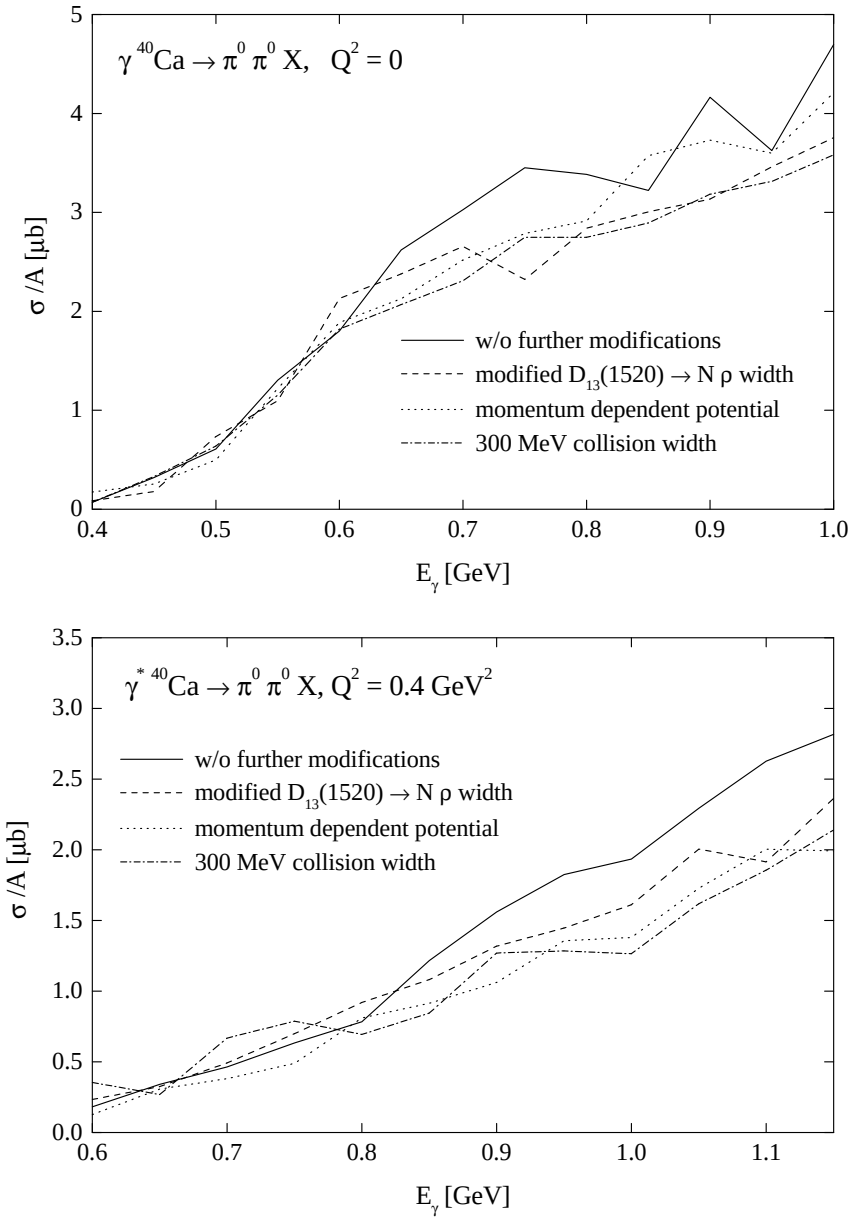

Figure 18: Cross section of the reaction $\gamma^{*40}\mathrm{Ca} \to \pi^0\pi^0 X$ for different Q^2. The medium modifications are explained in the text.

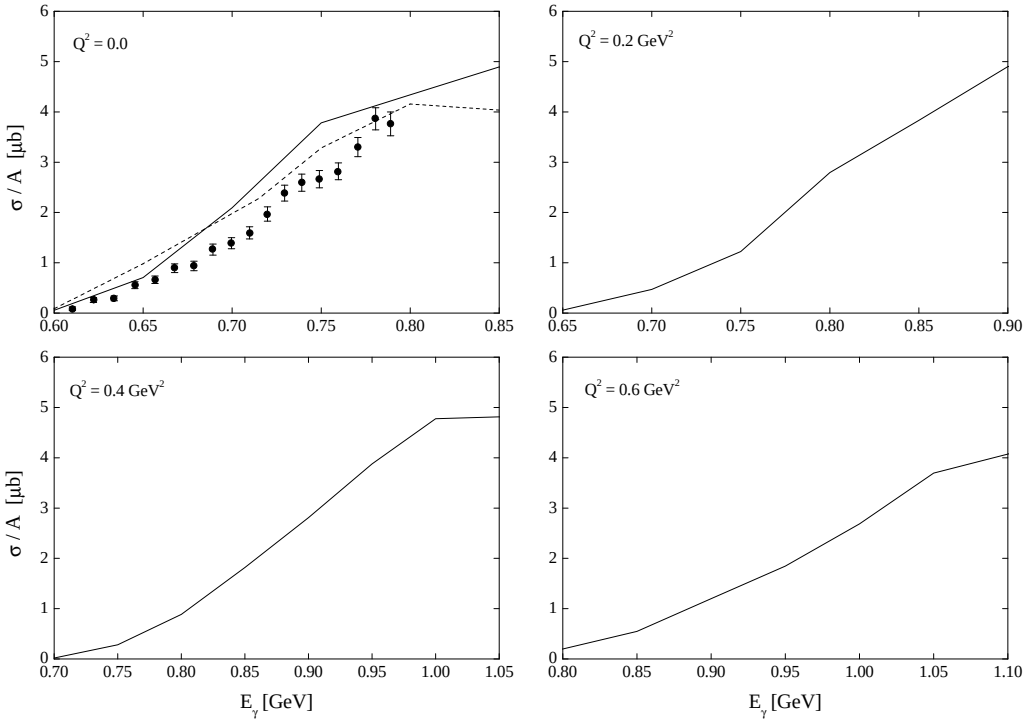

Figure 19: Cross section of the reaction $\gamma^{*\,40}\mathrm{Ca} \to \eta X$ for different Q^2. For $Q^2 = 0$ the dashed curve was calculated using the constant ηN cross sections. The data for $Q^2 = 0$ are from [34].

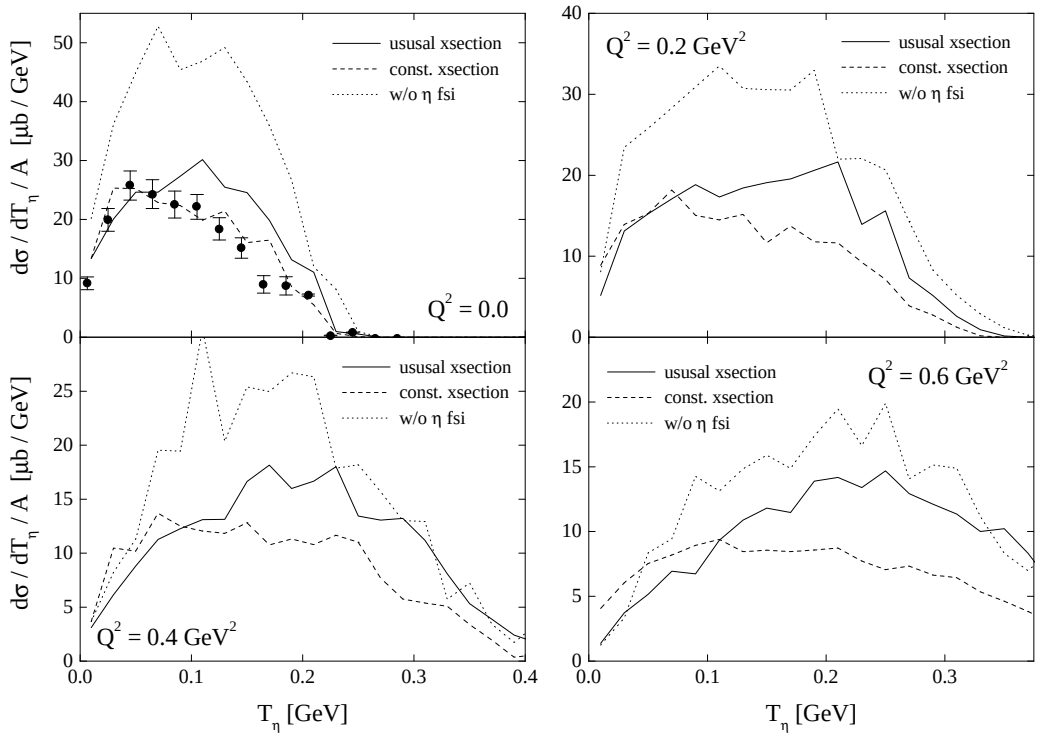

Figure 20: Energy differential cross section of the reaction $\gamma^{*40}\mathrm{Ca} \to \eta X$ for different Q^2 for $\sqrt{s} = 1.54$ GeV. The different curves are explained in the text. The data are from [34].

	^{12}C	^{40}Ca	^{208}Pb
r_0 [fm]	2.209	3.614	6.755
α [fm]	0.479	0.479	0.476

Table 1: Parameters r_0, α for the Woods-Saxon distribution.

	ε bin	$P_{33}(1232)$	$D_{13}(1520)$	$S_{11}(1535)$	$F_{15}(1680)$	1π	2π
a	$\varepsilon \geq 0.9$	1.06	0.65	1.07	0.7	1.0	0.6
	$0.6 < \varepsilon < 0.9$	1.0			0.6		
	$\varepsilon \leq 0.6$	1.03			0.45		0.65
b	$\varepsilon \geq 0.9$	1.85	1.25	3.0	2.0	2.5	1.95
	$0.6 < \varepsilon < 0.9$						
	$\varepsilon \leq 0.6$	1.8					
c	$\varepsilon \geq 0.9$	1.0	0.5	0.5	0.5	0.5	0.975
	$0.6 < \varepsilon < 0.9$						
	$\varepsilon \leq 0.6$						

Table 2: Parameters a, b und c for the form factors.